ELECTROCHEMICAL CHARACTERIZATION OF ORDERED MESOPOROUS CARBIDE-DERIVED CARBONS

A Thesis
Presented to
The Academic Faculty

by

Yair Korenblit

In Partial Fulfillment
of the Requirements for the Degree
Masters of Science in the
School of Materials Science and Engineering

Georgia Institute of Technology
August, 2009

ELECTROCHEMICAL CHARACTERIZATION OF ORDERED MESOPOROUS CARBIDE-DERIVED CARBONS

Approved by:

Dr. Gleb Yushin, Advisor
School of Materials Science and Engineering
Georgia Institute of Technology

Dr. David Bucknall
School of Materials Science and Engineering and
Polymer, Textile and Fiber Engineering
Georgia Institute of Technology

Dr. Alexander Alexeev
School of Mechanical Engineering
Georgia Institute of Technology

Date Approved: June 30, 2009

To my loving family and friends

ACKNOWLEDGEMENTS

I wish to thank Dr. Gleb Yushin for his support and insight into the field of electrochemical capacitors. I would like to thank my family, friends and co-workers, for all the great support that they provided, without which I would have not been able to complete this body of work. My gratitude goes to the research group of Dr. Stefan Kaskel (Technische Universität Dresden) for their collaboration on this research and our future research projects.

TABLE OF CONTENTS

LIST OF TABLES

LIST OF FIGURES

LIST OF SYMBOLS AND ABBREVIATIONS

SiC	Silicon carbide
EDLC	Electrochemical double-layer capacitors
CDC	Carbide-derived carbon
DFT	Density functional theory
BET	Brunnauer, Emmet, and Teller
$TEABF_4$	Tetraethylammonium tetrafluoroborate
SSA	Specific surface area
m^2/g	Meters squared per gram
HEV	Hybrid-electric vehicle
$/kJ	Dollars per kilojoule
C	Capacitance
Q or q	Charge
V	Voltage
ε_0	Permittivity of free space
ε_r	Relative dielectric constant
A	Area
d	Distance
F	Force
G	Free energy
r	Distance
λ	Fraction of charge
dG	Change in free energy

dq	Differential charge
dλ	Differential fraction
F	Farads
dv/dt	Voltage sweep rate, volts per second
R	Resistance
I	Current in amps
Wh/kg	Watt hour per kilogram
W/kg	Watt per kilogram
KOH	Potassium hydroxide
$ZnCl_2$	Zinc chloride
H_3PO_4	Phosphoric acid
H_2SO_4	Sulfuric acid
°C	Degrees Celsius
F/g	Farads per gram
MWCNT	Multi-walled carbon nanotubes
3D	Three-dimensional
RuO_2	Ruthenium oxide
H	Hydrogen
e^-	Electron
Al_4C_3	Aluminum carbide
ZC	Zinc carbide
TiC	Titanium carbide
B_4C	Boron carbide
$Ti_{2/3}AlC$	Titanium-aluminum carbide
Ti_3SiC_2	Titanium silicocarbide

Cl_2	Chlorine gas
C	Carbon
g	gas
TEM	Transmission electron microscope
C-D	Charge-discharge
A/g	Amps per gram
ESR	Equivalent series resistance
kg	Kilograms
J	Joules
Wh	Watt-hours
CV	Cyclic voltammetry
EIS	Electrochemical Impedance Spectroscopy
f	Frequency
Z”	Imaginary component of the impedance
Z’	Real component of the impedance
C’	Real component of the capacitance
C”	Imaginary component of the capacitance
τ_o	Time constant
ω	Angular frequency
f_{trans}	Transission frequency
Hz	Hertz
K	Kelvin
N_2	Nitrogen gas
CO_2	Carbon dioxide gas
nm	Nanometer

P	Pressure
V_a	Volume of gas adsorbed
CO_2	Carbon dioxide gas
RS	Raman spectroscopy
G	Graphite band
D,D',G'	Disorder bands
I_G	Integrated intensity of G band
I_D	Integrated intensity of D band
XRD	X-ray diffraction
θ	Angle of incidence
SAXS	Small-angle X-ray spectroscopy
SEM	Scanning-electron microscopy
Mw	Molecular weight
PTFE	Polytetrafluoroethylene
wt. %	Weight percent
µm	Micrometers
ppm	Parts per million
kHz	Kilohertz
mV	Millivolts
PSD	Particle size distribution
mg	Milligrams
CCD	Charge-coupled device
mA/g	Milliamps per gram

SUMMARY

Porous carbon derived from an inorganic silicon carbide (SiC) precursor, termed SiC-derived carbon, is an attractive material for electrochemical energy storage applications, including electrodes for electrical double layer capacitors (EDLCs). The objective of this thesis is to investigate the effects that the carbide-derived carbon (CDC) microstructure and pore structure have on the energy and power characteristics of the EDLC electrodes.

Conventional SiC CDC is produced from non-porous crystalline SiC powder at temperatures above 800 °C. Here we studied the performance of SiC CDCs produced by chlorination at 700-900 °C of an ordered mesoporous SiC precursor, which was synthesized via a 1000 °C pyrolysis of polycarbosilane infiltrated into an SBA-15 silica template having ordered mesopores. The SiC CDC was purified from chlorine impurities by annealing in ammonia. The surface area and pore size of the purified SiC CDC was characterized via N_2 and CO_2 sorption using density functional theory (DFT) and Brunnauer, Emmet, and Teller (BET) theory. The specific capacitance, power and energy densities were characterized via electrochemical measurements of the SiC CDC electrodes in 1 M tetraethylammonium tetrafluoroborate ($TEABF_4$) acetonitrile solution.

The SiC CDC exhibited a specific surface area (SSA) in excess of 2400 m^2/g and gravimetric capacitance values of up to ~ 150 F/g, among the highest ever reported for any electrodes in this electrolyte. The ordered mesopores allowed for fast ion transport within each particle, resulting in excellent capacity retention under high current rates and ultra-fast frequency response, thus allowing for extremely high power and energy

densities. The best overall performance was achieved in SiC CDC samples chlorinated at the lowest temperature of 700 °C.

CHAPTER 1

INTRODUCTION

1.1 Motivation

In recent times the population of the United States has felt the burden of increasing costs of hydrocarbon fuels. On a larger scale, discussions in regard to the adverse effects of heavy reliance on hydrocarbon fuels and the world's dependency on them have become more and more prevalent. The World Energy Outlook 2004 projects that by the year 2060 the world's energy demand will increase by 60% (1). The ability to mediate these developing problems lays in the development of technologies to alleviate the reliance on hydrocarbon fuels.

Developing countries are demanding increasing amounts of energy for transportation and industrial needs. In addition, consumers are demanding more and more energy and power from electronic devices and electrical machines. For instance, hybrid electric vehicles (HEV) are seeing increased power demands from consumers. Increasing energy usage at home results in problems of power quality and level maintenance. Maintaining the voltage levels and preventing what is known as voltage sags has been found to be the most common electrical disturbance in distribution systems (2). Electrochemical capacitor banks can provide the power necessary to alleviate these problems (3, 4).

Electrochemical capacitors are energy storage devices akin to a hybrid between batteries and capacitors. Their performance can be compared to other energy systems via a Ragone plot such as the one in figure 1.1. Electrochemical capacitors are currently

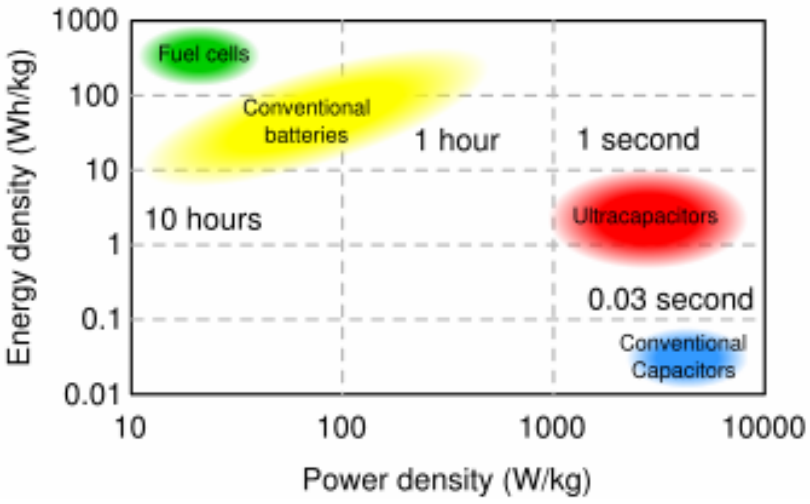

Figure. 1.1. Ragone plot comparing energy and power performance for a variety of systems (5).

produced by several companies including Maxwell technologies (US), ESMA (Russia), Elit (Russia), Tavrima (Canada), Panasonic (Japan), Ness Capacitor (South Korea), Epcos (South Korea), LG (South Korea), Samsung (South Korea) and others. The ability of electrochemical capacitors to provide a combination of high energy and power densities (figure 1.1) opens a broad range of applications. A cost comparison of dollars per kilojoule ($/kJ) in 2001 suggests that while batteries can provide energy at nearly thirteen times lower cost per kJ than an electrochemical capacitor, the power (energy delivered per unit time) of batteries can be at least three times more expensive nor can it provide the necessary power for many applications (6).

Lowering the cost of electrochemical capacitors or enhancing their power and energy characteristics will lead to the enhancement of the lives of individuals around the world and improve the health of our environment. Future and current applications, which will benefit from these enhancements, include memory backup, energy efficient hybrid engines, electric vehicles, high power electric tools, power quality, and many others.

Many of these applications are currently feasible yet are stymied by the high costs of electrochemical capacitors, especially, electrochemical capacitors with higher energy densities, which employ ruthenium oxide. Through continued research and investigation of low-cost synthesis methods and materials these costs are expected to drop and facilitate the incorporation of electrochemical capacitors into many commercial and military technologies (7). Continued research will improve the understanding of underlying chemical and physical operation principles and allow for significant improvements in device performance. By distributing the energy and power storage demands of the world to a variety of technologies, such as fuel cells, batteries, flywheels and electrochemical capacitors, the world's energy problems can be mitigated and global energy sustainability can be improved.

1.2 The History of Electrochemical Capacitors

In 1957 Becker patented an energy storage device based on a porous carbon utilizing an aqueous electrolyte, an electrochemical capacitor (8). In 1966 the Sohio Corporation in Cleveland, Ohio created a similar device utilizing a non-aqueous solution that permitted for higher operating voltages and thus higher energy densities (9). In 1971 Trasatti et al reported the interesting capacitance performance of an expensive metal oxide, ruthenium oxide(10). In 1975 B. E. Conway used faradaic reactions and the potential dependence of electrochemical adsorption of monolayers of base metals such as lead, bismuth, and copper on noble metals and the redox reactions associated with ruthenium oxide in sulfuric acid to create significantly higher energy density electrochemical capacitors as compared to that designed by Becker's carbon electrochemical capacitor (11).

Becker's technology and that of those who followed him relied on a physical phenomenon that was first modeled half a century earlier by Hermann von Helmholtz (12). These storage devices are now known as electrochemical capacitors, supercapacitors and ultracapacitors. The mechanism allowing for their energy storage is that of the double layer or the double layer combined with surface redox reactions (in aqueous solutions and mostly with metal oxides). The double layer arises in all solid/electrolyte interfaces and phase boundaries between two immiscible electrolyte solutions.

Helmholtz modeled the distribution of ions near the surface of the electrode. His model described charge on one side of the electrode separated by several nanometers from the opposing charges provided by the dense layer of solution ions in which the electrode is immersed. The foundation for this model lay in the operating principles of the parallel plate capacitor. In actuality the phenomenon of charge storage at a surface was not new in Helmholtz's time, either. Static charge on the face of amber was acknowledged during ancient times and the scientific studies from that era to modern times were necessary to decipher the mechanisms underlying the operation of electrochemical capacitors. Studies had to be undertaken in the molecular theory of electricity, the electron theory of metals, solvation, diffusion, and electrical and ionic conduction. The major bodies of work to uncover these mechanisms entailed the research of Michael Faraday, Joseph John Thompson, and Robert Andrews Millikan. Through their work our understanding of parallel plate capacitors and the Leyden jar was made possible. The Leyden jar, attributed to Ewald Jurgens von Kleist and Pieter van Musschenbroek from Leyden, was a glass jar in which was an aqueous electrolyte that

had an immersed electrode and on the outside a metal foil. The jar allowed for charge storage and separation via a glass dielectric. It was later known as a "condenser," and finally as a capacitor. With time other dielectrics were used such as air, vacuum, polystyrene, mica and many other materials.

Following the original work of Helmholtz, Gouy and Chapman had considered that the thermal motion of the ions in solution would lead to a diffuse layer of adsorbed ions, rather than a dense layer as described in Helmholtz's original treatise. After Gouy and Chapman's work, Stern then provided a modification that took into account the fact that ions in solution are not ideal point charges and allowed them to have volume. As a result, the center of the ions resided at a distance from the metal (electrode) surface while utilizing the distribution modeled by Gouy and Chapman. The last fundamental modification to this developed theory was made by Grahame in 1947. Grahame used the information gained from studying the structure of the electrolyte to elucidate that the metal/solution interaction leads to different planes of closest approach for the ions depending on their solvation-state and surface interaction. This finalized the Gouy-Chapman-Stern-Grahame model of the electrical double layer. The qualitative model most accepted for the description of this phenomenon. As time progressed, further enhancements were made by theoreticians to adjust for realizations made with time that were not available to the ground-breaking researchers who came before them. It is worth noting that in many instances technology comes before a deep understanding of theory is available, but in the case of electrochemical capacitors, it was the theory that propagated the advancement and proliferation of the technology (11).

1.3 Principles of Operation

The following sections provide a description of the physical processes underlying the operation of electrochemical capacitors. Since the inspiration for the model given by Helmholtz came from the understanding of parallel-plate capacitors, or electrostatic solid-state capacitors, that technology will be used as a starting point for the explanation of electrochemical capacitor operation.

1.3.1 Parallel-Plate Capacitors

The most common electrostatic capacitors are generally constructed out of two metal plates, separated by vacuum or dielectric materials, such as air, water, barium titanate, and silicon dioxide (13). Figure 1.2 shows a simplified response of the dielectric material and a generalized setup for a solid-state parallel-plate capacitor under bias.

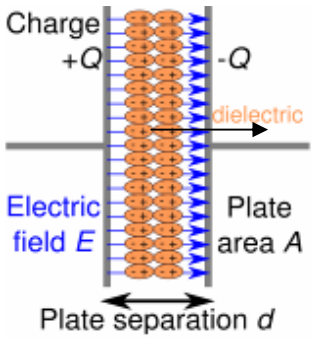

Figure 1.2. Solid-state capacitor (14).

When the bias is removed, the charge/energy is stored, and upon closing of the circuit the energy is released, mainly in the form of electric current flow. The ability of the system to store charge upon application of a potential is a measure of its capacitance (not to be mistaken for a battery's ability to store charge – known as capacity). Capacitance (C) is defined as follows

$$C = \frac{Q}{V} \text{(farads)} \quad (1.1)$$

$$C = \varepsilon_o \varepsilon_r \frac{A}{d} \text{(farads)} \quad (1.2)$$

Q is the amount of charge (coulombs) on one plate and V (volts) is the potential difference applied to the two plates. The unit of capacitance is a farad which is equivalent to coulombs per volt. The capacitance can also be determined by the area of the plates (A), multiplied by the relative dielectric constant (ε_r, unitless), also known as the relative static permittivity of the material between the plates. This is multiplied by the permittivity of free space (ε_0 - 8.85×10^{-12} F/m based on using meters for the plate distance and area), divided by the distance between the plates (d). The key factors for performance control in such a device are the distance between the plates, the dielectric constant, and the area of the plates (11, 12). The relative permittivity factor represents the ability of the material to transmit an electric field and is affected by the behavior of the material under a polarizing field (11). As the material is subjected to the electric field, it has several polarization mechanisms that may take place, which include electronic, ionic, dipolar, and space charge polarizations. These mechanisms are frequency dependent (see figure 1.3) and may be pronounced in different amounts in different materials, for instance polar liquids have more tendency to reorient than non-polar liquids (11).

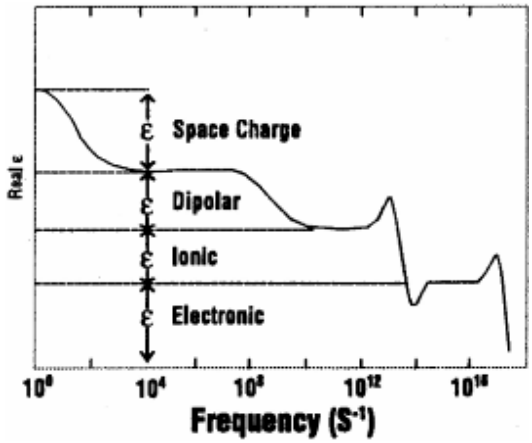

Figure 1.3. Polarization mechanisms and their frequency dependence (15).

Electronic refers to the displacement of the electronic cloud relative to the positive core. Atomic refers to separation of positive and negative ions with respect to one and other. Orientational involves the alignment of dipoles with the electric field. Finally, space charge involves the presence of charges impeded by interfaces, or trapped in the material. These polarization mechanisms result in the storage of energy in the dielectric material, resulting in an increase in the capacitance of the device employing them (16).

Capacitance accounts for the different energy storage mechanisms taking place, and can be used when calculating the total energy stored. It is possible to derive an expression for the free energy of an electrode by considering that as the capacitor is charged, more and more of the same charges are brought to the electrode plates and are experiencing increasingly repulsive forces. Through Coulomb's law (employing the dielectric constant) it can be seen that

$$F = \frac{Q_1 Q_2}{4\pi\varepsilon_o \varepsilon r r^2} \quad (1.3)$$

$$G = \frac{Q_1 Q_2}{4\pi\varepsilon_o \varepsilon r r} \quad (1.4)$$

The force F (Newtons) is the repulsive force felt by the (same sign) charges Q1 and Q2 (coulombs), which are separated by distance r. G (Joules) is the Gibbs free energy available from this interaction. As the capacitor is charged, charges of the same sign are added to the same plate, which repel one and other. This increases the energy of the system. By considering a fraction λ of the total charge q (ultimately reaching λ=1), we can perceive the plates as being charged progressively with λq. Now if we consider an infinitesimal charge δq added to the electrode, we can calculate the incremental increase of free energy in the electrode dG by considering that the potential energy added to the system under a potential V to a charge q is qV, and that V can be found by dividing the amount of charge by the capacitance C.

$$dG = \frac{\lambda q}{C} dq = \lambda V dq \qquad (1.5)$$

$$dq = q d\lambda \qquad (1.6)$$

$$\Delta G = \int_0^1 \frac{\lambda q}{C} \; \mathrm{q d}\lambda \qquad (1.7)$$

$$= \frac{1}{2}\frac{q^2}{C} = \frac{1}{2} C V^2$$

1.3.2 Electrochemical Capacitors

Electrochemical capacitors are known as supercapacitors, ultracapacitors, and several other names originating from their military and commercial applications (17, 18). They consist of electrical contacts (also called current collectors, shown in figure 1.4 as grey metallic plates on the left and right sides of the electrochemical capacitor) upon which active electrode material is placed. The conventional device is symmetric and the two current collector – electrode modules are separated by a membrane. The membrane (shown as a semi-transparent block in the center of the capacitor in figure 1.4) prevents

electrical shorting but allows ion migration (see figure 1.4). The electrode assembly is immersed in a solution of electrolyte ions. Upon application of a potential, positive ions move towards the negative electrode and negative ions towards the positive electrode, adsorbing on the internal surface of the active material particles (figure 1.4).

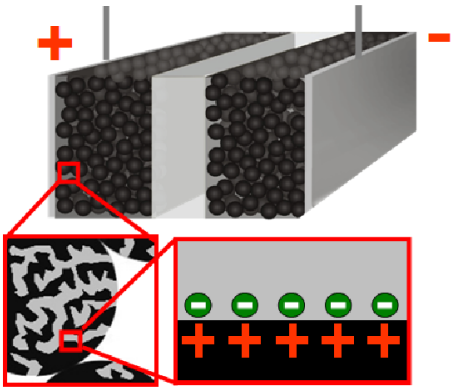

Figure 1.4. Schematic of electrochemical capacitor.

The research initiatives in the electrochemical capacitor field mainly focus on the electrode material, the electrolyte solution, which could be aqueous, organic, and/or ionic liquid and the separator materials, which are often made of cellulose, Teflon, or other polymers (19). The electrolyte employed is generally the limiting constraint of the voltage operation limit of the device, although, unwanted redox reactions of the electrode material may be the cause in some instances. In addition, the conductivity of the electrolyte can have a significant impact on the power performance of the device. Most electrochemical capacitors operate between 1 to 5 volts (20, 21). Table 1.1 lists some properties of electrolytes used in electrochemical capacitors. Electrochemical capacitors are traditionally categorized into two different types, electrical double layer capacitors (EDLC) and pseudocapacitive capacitors (11).

Table 1.1. Comparison of electrochemical capacitor electrolytes.

Electrolyte System	Pros	Cons
Aqueous	Non-toxic potential, low-cost, high energy density faradaic reactions	Low operating potential limit < 1 V, highly studied sulfuric acid solution considered unsafe
Organic	Higher operation potential ~2.5 V, high power possible	Lower energy density, flammable, toxic, moisture sensitivity
Ionic Liquid	High operating voltage (up to 5 V), easy handling, reduced flammability	Lowered power due to large ion size

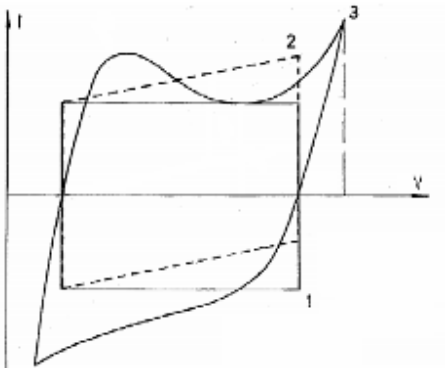

Figure 1.5. Schematic of typical electrochemical capacitor charge/discharge (22) 1 – ideal capacitor, 2 – capacitor with resistance, 3 – non-ideal capacitor.

Figure 1.5 shows the general characteristics observed by electrochemical capacitors in cyclic voltammograms. If the following equations are considered it can be seen why a rectangular shape is expected from ideal capacitors.

$$C = \frac{dq}{dv} \qquad (1.8)$$

$$I = \frac{dq}{dt} \qquad (1.9)$$

$$C = \frac{Idt}{dv} = \frac{I}{dv/dt} \qquad (1.10)$$

C is the capacitance (F), dq is the differential charge (Coulomb), dv is the differential potential change (V), dt is the differential time change (sec), and I is the current (amps). If the sweep rate (dv/dt) is kept constant, and the capacitance is independent of voltage, then the current response should also remain constant throughout the charging/discharging process, and maintained at the same level for both charge and discharge (see 1 in figure 1.5). If the capacitor is non-ideal and a resistance is present (R), a dependency of the current (I) on potential (V), such as the one seen in ohm's law

$$V = IR \quad (1.11)$$

would account for the linear increase in current as the potential is increased, and decrease when the potential is decreased (see 2 in figure 1.5). The peaks which might appear in a non-ideal capacitor (see 3 in figure 1.5) are due to individual oxidation and reduction peaks, which cause a large deviation in charge (current) exchange. The voltammogram (figure 1.5) often has a mirror image response, which is representative of the high reversibility afforded by electrochemical capacitors. It can also be seen that as the direction of sweep is changed, there should be an immediate reversal of the current direction according to equation 1.10. The mirror-image symmetry is maintained as long

as there are no diffusion controlled processes. In the last case different potentials might be required for the anodic and cathodic currents to equalize, and the appropriate diffusion gradients need to be taken into account to predict the shape of the voltammogram (11).

The energy and power densities are two of the most important characteristics of electrochemical capacitors. Energy density is a measure of the amount of charge/energy storage a capacitor is able to hold per mass/volume of electrode material. Power density is a measure of the rate at which stored energy can be delivered. The power density depends on both the energy density and the time or frequency response of an electrochemical capacitor. The faster the capacitor can be charged/discharged the higher the power response. Table 1.2 compares standard performance characteristics of solid-state capacitors, electrochemical capacitors, and battery systems.

Table 1.2. Comparison of Standard Energy Storage Systems (23).

Characteristic	Lead-Acid Battery	Electrochemical Capacitor	Conventional Capacitor
Charge Time	1 to 5 hrs	0.3 to 30 sec	10^{-3} to 10^{-6} sec
Discharge Time	0.3 to 3 hrs	0.3 to 30 sec	10^{-3} to 10^{-6} sec
Energy density (Wh/Kg)	10 to 100	1 to 10	<0.1
Cycle Life	1000	>500000	>500000
Power density (W/Kg)	>100	>1000	>10000

1.3.3 Electrical Double Layer Capacitors

The term double layer was coined by Helmholtz in 1857 (24). When a conductor is placed in a solution of ions and a potential bias is applied electric charge resides on one side of the electrode and ions (of the opposing charge) adsorb on the other side (electrolyte side) of the metal-solution interface (see figure 1.4), thus termed the double layer. This occurs at the opposing electrode, with the sign of the charges reversed (11). This means that for symmetric, commercial EDLC two capacitors are operating in series (since there are two electrodes), which results in an approximate halving of the capacitance as compared to a single electrode's capacitance. The solution ions in an ideal EDLC are adsorbed onto the surface and do not involve any chemical reactions (Faradaic reactions), such as those that take place in a battery. This allows for a significantly larger number of charge/discharge cycles (>500,000) compared to popular battery systems (<1000) (12, 25). Figure 1.6a is a schematic demonstrating the double layer concept as modeled by Helmholtz. Over time other scientists have modified this model to better explain the distribution of ions relative to the electrode surface, as seen in figure 1.6b (26-30).

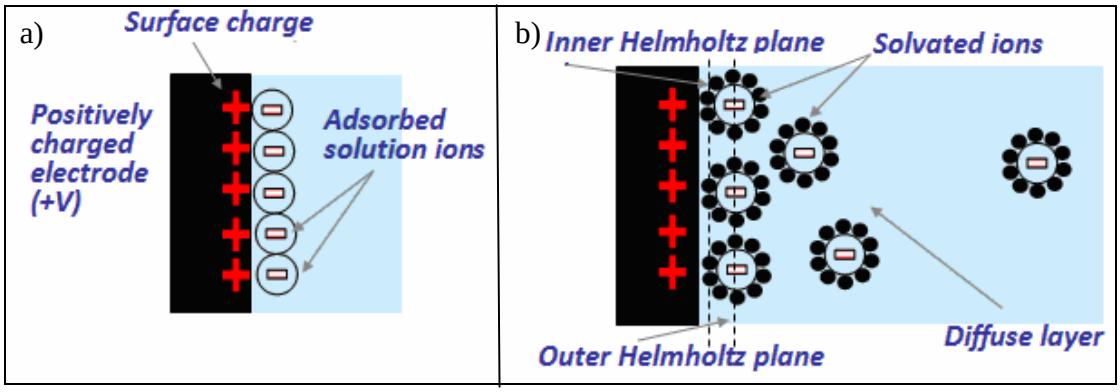

Figure 1.6. (a) Schematic of the model proposed by Helmholtz (b) Schematic of the Guy-Chapman-Stern model (1).

Since the total capacitance largely depends on the surface area, commercial EDLC commonly employ conductive, high-surface area materials, such as porous carbons with well developed porosity, for example activated carbons. These high-area carbons can be made of inexpensive materials such as coconut shells, corn, sugars, and other precursors such as polyacrylonitrile, penolic resin, petroleum coke, anthracite, pitch, and coal (31-38). The activation process is generally divided into two categories: thermal/physical or chemical. The first step in producing activated carbons in both categories involves carbonization of a precursor (removal of non-carbon species by thermal decomposition in an inert atmosphere). The second step is different for both categories. Thermally produced activated carbons require gasification - development of porosity by partial etching of carbon during annealing with an oxidizing agent, such as CO_2, H_2O, or a mixture of agents at moderate temperatures (below 400 °C). Production of activated carbons by chemical activation generally involves the reaction of the resulting carbon with a chemical reagent (KOH, $ZnCl_2$, H_3PO_4, H_2SO_4) at elevated temperatures (above 500 °C) (39-41). The purpose of the second step is to oxidize and remove part of the carbon, thus leaving pores and increasing the surface-area up to ~ 3000 m^2/g. Activated carbons having surface areas in excess of 2000 m^2 / g have demonstrated capacitance of up to 300 F/g in aqueous electrolytes (1, 21, 42, 43).

The activation process does not result in a tight pore size distribution, which makes it hard to study the effect of pore size on electrochemical performance (44). Additional carbons being studied as electrode materials for electrochemical capacitors include templated carbons (45-47), carbon nanotubes (48-50), nanodiamonds (50), cloths (51), fibers (51), and other high area carbons, including CDCs (50-53). Different

structures and morpohology provide different performance characteristics. These differences are due to several parameteres, including pore sizes, pore shapes, crystal structure, and particle sizes. For instance, a high surface area of activated carbons leads to an increased specific capacitance, but the complex pore structure entailing bottleneck pores may significantly hamper the frequency response of the EDLC based on activated carbons and allow for modest power density characteristics. Carbon onions and multi-walled carbon nanotubes (MWCNT) have lower surface areas than the high capacitance activated carbons, but their open pore structures allow for much faster charging and discharging, leading to better power performance (50). In addition, the high electrical conductivity of MWCNT, as compared to activated carbons, facilitates further increase in power density (43). However, the gravimetric capacitance of MWCNT and carbon blacks is generally <50 F/g, while the capacitance of activated carbons and templated carbons can reach 300 F/g (54). Templated carbons (45-47), with a template-determined porosity may offer a combination of high capacitance and good frequency response, thus leading to high energy and power density.

Until recently it was believed that the pore size should be on the order of two to three times larger than the size of the solvated ion in order to utilize the surface area of those pores (55, 56). New evidence reported by Chmiola et. al. demonstrated that sub-nanometer pore sizes, which are attainable through templated carbons and CDC, can lead to higher capacitances than those achieved by activated carbons (57-59).

1.3.4 Pseudocapacitors

Significantly higher capacitances are attained if use is made of electrochemical reactions such as those obtained by employing metal oxides in aqueous electrolytes. The

energy storage mechanism, titled pseudocapacitance, is attributed to fast and highly reversible surface chemical (faradaic) reactions. In reality reactions are not completely reversible, not necessarily limited to the surface and result in faster capacitance fading, meaning cyclability is not as high as compared to double layer capacitors employing carbon. These charge transfer reactions, no matter their limitation to the surface and cyclability, store a significantly larger amount of energy in the electrode, as compared to the ion physisorption taking place in double layer capacitors (11, 51). Unlike the 3D bulk reactions which transpire in battery chemical reactions, it is mostly accepted that the reversible reactions occurring in pseudocapacitors are 2D, and do not entail a phase change (48, 60). In addition, many of the reactions at the surface of a pseudocapacitor take place over a range of potentials and faradaic processes, unlike the pronounced individual faradaic peaks that occur in batteries (11). This results in the pseudocapacitor voltammogram having a fairly potential independent current response (61). Figure 1.7 shows the contrast between batteries and electrochemical capacitors via examination of their voltammograms (11). Figure 1.7a shows the current-voltage (referenced to the reversible hydrogen electrode) response curve for an electrochemical capacitor (in this case ruthenium oxide), and figure 1.7b shows a typical response curve for a battery (lead/lead chloride). The electrochemical capacitor I-V curve shows a mirror-image response for the different sweep directions (typical of capacitor systems), and an almost immediate reversal of current upon direction change. Although not illustrated in this voltammogram, the capacitance of this metal oxide does not display a strong dependence on voltage sweep rate. In some electrochemical capacitors the presence of micropores and large diffusion distances are expected to result in a sweep rate dependence for the

capacitance (62). The battery on the other hand, does not show a mirror image voltammogram (figure 1.7b), does not change current direction immediately, and requires significant overvoltages in both sweep directions resulting in a separation of the oxidation and reduction peaks. The semi-rectangle formed by the pseudocapacitor I-V curve (figure 1.7a) is attributed to multiple redox reactions occurring over varying potential ranges that result in a fairly constant charging current at a constant sweep rate (11).

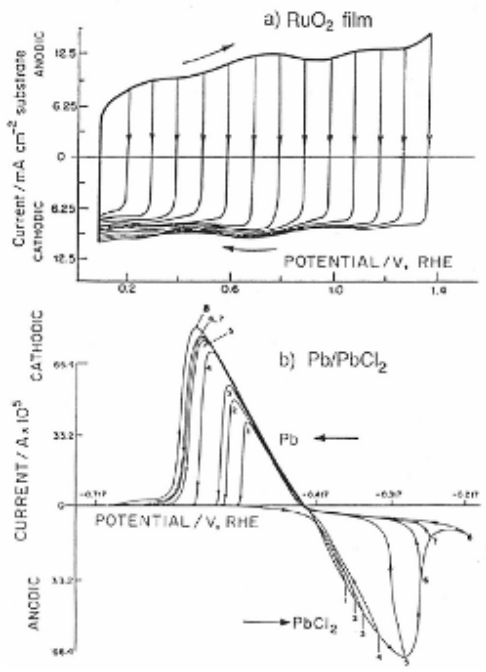

Figure 1.7. Typical cyclic voltammograms of (a) supercapacitors and (b) batteries (11).

The power density of electrochemical capacitors is inversely related to their resistance (63). The energy density increase provided by metal oxides usually comes with a cost in power density since there is a dependence on the slower faradaic reactions and metal oxides have low conductivity, which reduces the power density of the electrochemical capacitor as compared to carbon-based electrochemical EDLC. As a result, commercial pseudocapacitors are constructed using the expensive ruthenium

oxide, which is fairly conductive for a metal oxide. Thus far, most research efforts have focused on ruthenium oxide, iridium oxide, and manganese oxide (64, 65).

Research into the mechanisms involved in metal oxides, such as ruthenium oxide has resulted in some mechanism suggestions (chemisorption reaction described below), but research into the field continues (11, 66). The suggested chemical reactions for RuO_2, which may be similar to the mechanisms in MnO2 and IrO2 is (60, 66) (forward for charging, backward reaction for discharging).

$$RuOOH \leftrightarrow RuO_2H_{1-\delta} + \delta H^+ + \delta e^- \text{ (anode)}$$
$$RuO_2 + \delta H^+ + \delta e^- \leftrightarrow RuO_{2-\delta}H_{1-\delta} \text{ (cathode)}$$
$$0 \le \delta \le 2$$

In aqueous solution, on the cathode side, a proton approaches the surface of the ruthenium oxide electrode, and when a potential is applied, an electron is accepted. Hydrogen is then chemisorbed onto the surface of ruthenium oxide. On the anode side, a lower oxidation state is more energetically favorable to participate at which point a proton can be released, and an electron along with it.

The morphology and crystal structure of the metal oxide in use has been demonstrated to be of extreme importance. There appears to be magnitude differences in energy and power density when ruthenium oxides and manganese oxides are in a hydrated amorphous state, as compared to their non-hydrated crystalline state (61, 67). In addition, since pseudocapacitance is primarily attributed to surface reactions, it is reasonable to expect that an increase in the surface area of the metal oxide will result in an increase in capacitance, as is seen in the case of hydrated amorphous ruthenium oxide (61). Although pseudocapacitance is primarily accepted as a surface reaction, there have

been reports of diffusion into particles, also known as intercalation. Such reports involved hydrated amorphous ruthenium oxide and hydrated amorphous manganese oxide (in which charging remained reversible and did not entail a phase change), and demonstrated that energy and power density had a dependency on particle size (61, 67).

A group of materials that are of great interest for pseudocapacitors are conducting polymers. The most studied conductive polymers are polythiophene, polypyrrole, and polyaniline (22, 68-72). The storage mechanism is that of doping and on discharge de-doping of the polymer backbone. Like some of the metal oxides, cyclability is hampered due to some irreversible side-effects of this mechanism such as structural instability.

1.4 Cell construction

The construction and design of the electrochemical capacitor can cause variations in the electrochemical performance. For instance, inaccessibility to solution, bad interfacial contacts, thermal management and more issues can arise due to incorrect design. Commercial devices have several common designs including spiral wound and monoblocks (73, 74). The spiral-wound design is very similar to standard battery production methods and the monoblock design entails cells that consist of many positive and negative electrodes in parallel in order to increase the available cross-sectional area. Figure 1.8 and Figure 1.9 illustrate the construction of these two types of commercial electrochemical capacitors.

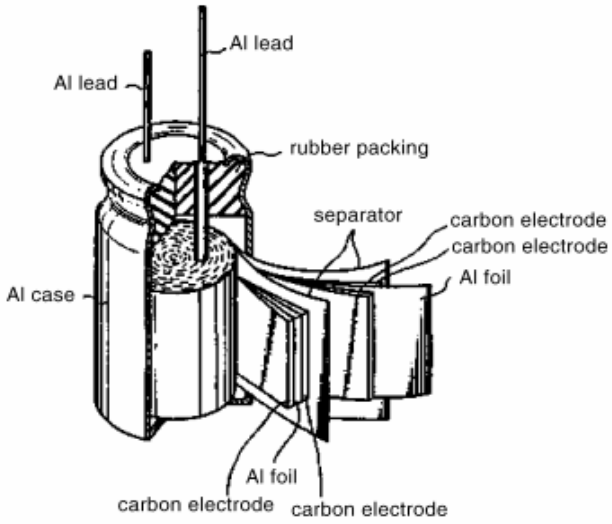

Figure 1.8. Schematic view of a Panasonic EDLC (74).

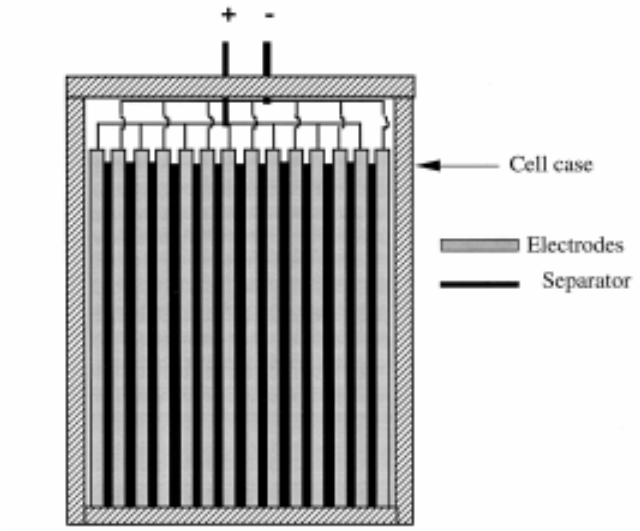

Figure 1.9. Cross-section of monoblock EDLC (73).

In addition to these designs there is also an all-solid design which can enhance the safety providing safer handling and reduction in flammability(75, 76).

1.5 Carbide-Derived Carbons

CDCs are porous carbons with sub-angstrom controllable pore sizes from around 0.5 to 2 nm and less controllable mesopores (77). They have found applicability in many

different fields including extraction/purification of gases (78), tribology (79), hydrogen storage (80), protein adsorption (81), water purification (82), and electrochemical capacitors (83). Carbons from metal carbides are produced by etching the carbides, typically, via chlorine gas and it is possible to use other halogens like Br2, F2, ClF3 and others (84). Metal chlorides were being produced via chlorination of carbides as far back as 1918 (84), in the 50's attention was given to the resulting carbon by-product and in the 70's an investigation into the carbon resulted in the determination of its porous nature (85). The possible resulting carbon structures include amorphous carbon, nanocrystalline graphitic carbon, carbon nanotubes, carbon onions, nanocrystalline diamond, turbostratic graphite, and highly ordered graphitic carbon(86, 87). The structure and porosity of the carbide-derived carbons are dependent on various synthesis parameters including carbide precursor, etching temperature and halogen (88). Some of the studied carbides include Al_4C_3 (89), ZC (90), TiC(91), B_4C (92), Ti_2AlC (93), Ti_3SiC_2 (94), Ti_3AlC_2 (95), and SiC (96). The general reaction associated with the synthesis of CDCs via chlorination is (97)

$$MC_x(s) + (y/2)Cl_2(g) \rightarrow xC(s) + MCl_y(g)$$

The reaction is applied at temperatures between 200 and 1200 °C (97). Figure 1.10 illustrates the effect of the chlorination on a silicon carbide structure and figure 1.11 demonstrates the progressive change via transmission-electron microscopy (TEM) on a SiC whisker.

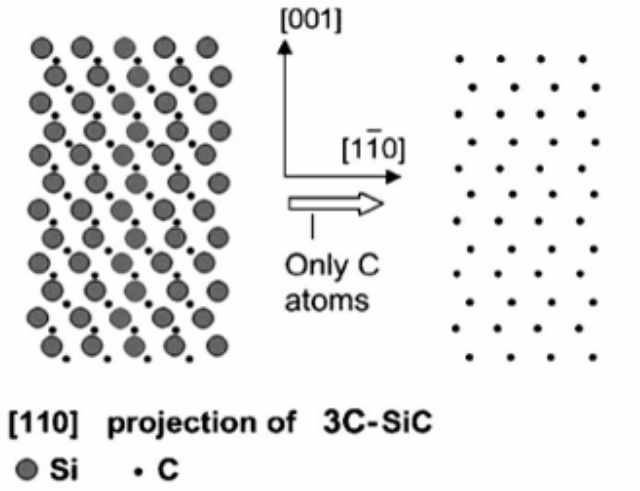

Figure 1.10. Two-dimensional schematic showing a SiC lattice pre and post etching (87).

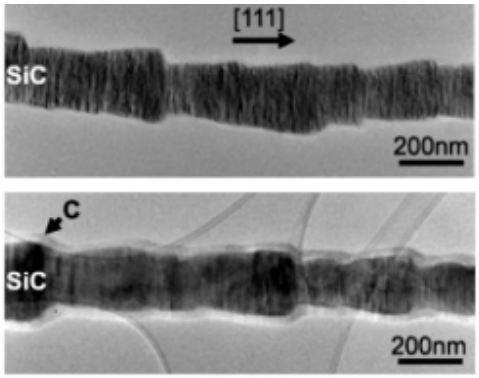

Figure 1.11. TEM image illustrating the gradual conversion of a SiC whisker to C (86).

The resulting carbons can have uni-modal pore size distributions like that seen in ceramic molecular sieves (88), which allows for engineering the materials to the appropriate application and also helped demonstrate the anomalous increase in capacitance when having pores equal to or smaller than the solvated ions used in an electrochemical capacitor (77). It is known that a combination of high surface area and micro and meso-sized pores can lead to high power and high energy density electrochemical capacitors. The tuneability of the pores and the fact that SSA's as high as

2000 m^2/g have been attained make CDCs extremely promising materials for electrochemical capacitors (98).

1.6 EDLC Characterization Methods

Important performance qualities of electrochemical capacitors include specific capacitance, energy density and power density. These characteristics are modulated by various parameters including the materials used for the electrode, the electrolyte, interfacial resistances, the separator membrane, and cell design. This study is focused on the effect of parameters varied during synthesis of the active electrode material. The study will attempt to explain correlations between properties like surface area, pore morphology, sizes and distribution and electrochemical performance. In order to characterize this performance, electrochemical testing including charge-discharge (Galvanostatic), cyclic voltammetry and impedance spectroscopy were employed and techniques like x-ray diffraction, scanning electron microscopy, and gas sorption techniques were used to examine the physical properties of the material.

1.6.1 Galvanostatic Test

Galvanostatic testing applies a constant current to the electrochemical capacitor using a galvanostat and the resulting voltage change with time is measured. This results in charging of the capacitor up to a pre-set voltage. The capacitor is then discharged and the voltage drop with time is measured. A typical charge-discharge (C-D) graph is illustrated in figure 1.12.

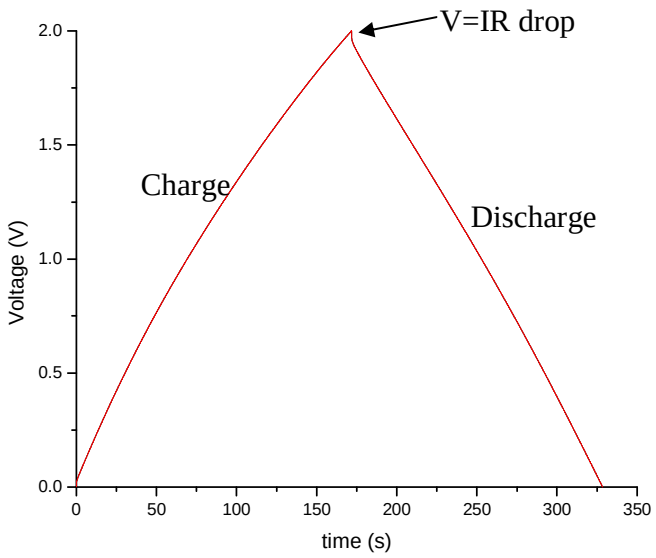

Figure 1.12. Galvanostatic (C-D) graph of CA29 at 0.8 A/g resulting in 113 F/g.

In figure 1.12 the device has a fairly low IR (potential) drop due to its low internal resistance or, as it is commonly termed, equivalent internal series resistance (ESR). This technique allows for a determination of the equivalent internal series resistance by quantifying the drop upon discharge (V=I*ESR). The ESR has several contributions to it including the electrical resistance of the carbon electrodes, the interfacial resistance between the current collectors (contacts) and active electrode mass, and ionic resistance of the electrolyte. The C-D test provides information on the (specific) capacitance of the device (F/g), energy density (Wh/kg), power density (W/kg), ESR (Ohm) and the affect of current density on these characteristics. Using equation 1.10 to find the capacitance of the total device, then dividing it by two since there are two electrodes working in series (and assuming they are the same) and then normalizing it by the mass of one electrode one can calculate the gravimetric capacitance. The energy density in Ws/g is obtained by using equation 1.7 and normalizing it to the mass. It is then multiplied by 1000 (for kg)

and divided by 3600 (1Wh=3600J) to get Wh/kg. To get the power (W/kg) the value in Ws/g is multiplied by 1000 and divided by the discharge time in seconds. Figure 1.13 is a Ragone plot showing power vs. energy density. As the charge-discharge happens at higher rates the power increases, but the energy density is reduced due to the inability of the ions to respond quickly enough to form the double layer and/or allow for the necessary faradaic reactions to take place.

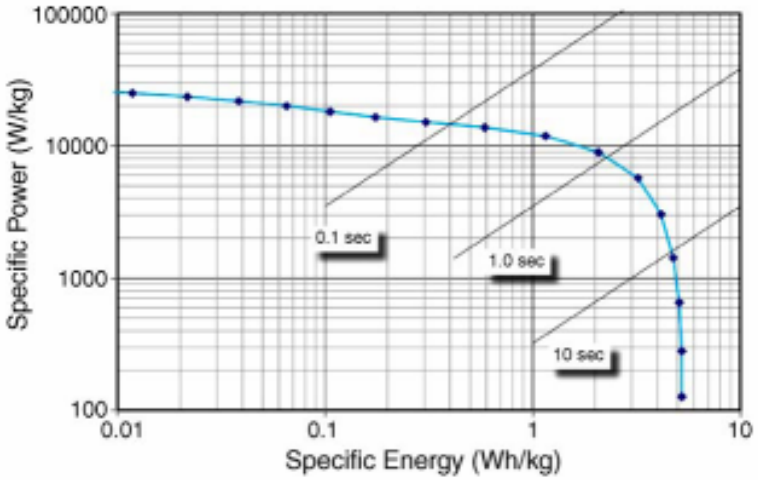

Figure 1.13. Ragone plot of a commercial 350 F capacitor (BCAP0350 Maxwell Technologies) (99).

1.6.2 Cyclic Voltammetry

Cyclic voltammetry (CV) is an electrochemical characterization technique involving the current response of a device with respect to a voltage change. This measurement applies a constant sweep rate (dv/dt) and monitors the current response of the two-electrode device. The sweep was done at varying rates to see the effect on capacitance and at various potential ranges, wherein the electrolyte remains stable. The information gathered from this characterization technique includes the (specific) capacitance (via equation 1.10 using the average current calculated by integrating the area and diving by the voltage range), effect of sweep rate on capacitance, and possible

information on the resistance/response of the device based on the shape of the cyclic voltammogram. For instance, as seen in figure 1.5, the ideal shape of a capacitor (rectangular) is often not seen due to possible faradaic reactions and the linear increase in current is due to the device's resistance. In this investigation the use of two-electrode cyclic voltammetry and mostly double-layer capacitance associated with carbon results in fairly symmetric voltammograms, excluding the current increase with increasing potential.

1.6.3 Electrochemical Impedance Spectroscopy

Electrochemical impedance spectroscopy (EIS) evaluates the electrochemical response of the electrochemical capacitor to an AC signal at various frequency rates. Generally, the response is plotted in the form of a Nyquist plot as illustrated in Figure 1.14. From the imaginary part of the impedance the capacitance vs. frequency response can be extracted using the following equation

$$C' = -\frac{1}{2\pi f Z''} \qquad (1.11)$$

The ESR of the device can be found by looking at the impedance value at the point at which the graph intersects the x-axis (see figure 1.14).

It should be noted that information regarding the interfacial contact resistance between the contact and electrode can be quantified by using the diameter of the semi circle formed at high frequencies (not seen in figure 1.14, but in data section).

In addition, when looking at the imaginary component, or dissipative component of the capacitance via equation 1.12 below, the maximum corresponds to a transition frequency between the capacitive (low frequency) and purely resistive (high frequency)

regimes of operation (100). The inverse of this transition frequency corresponds to a time constant τ_o, which provides an approximate measure of the appropriate frequency for utilization of the material and its performance relative to other materials.

$$C'' = \frac{Z'(\omega)}{\omega |Z(\omega)|^2} \qquad (1.12)$$

$$f_{trans} = f_{C''\max} \qquad (1.13)$$

$$\tau_0 = \frac{1}{f_{trans}} \qquad (1.14)$$

At frequencies between 1 and 100 Hz the graph has a 45° slope and is associated with the ions infiltrating the porous carbon structure. It is termed the distributed resistance regime. At low frequencies The graph attains an almost vertical shape and behaves much like an ideal resistor and capacitor in series and is no longer frequency dependent like it is at higher frequencies (99).

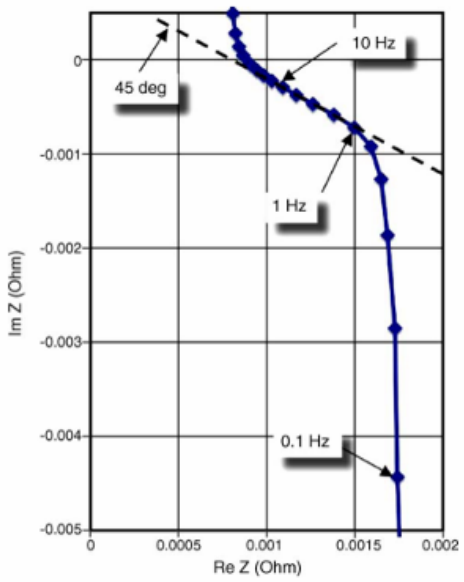

Figure 1.14. Nyquist plot of the impedance behavior of a 350 F capacitor (BCAP0350 Maxwell Technologies) (99).

1.7 Material Characterization Methods

1.7.1. Gas Sorption

Surface area and pore sizes of EDLC electrode materials are critical parameters for EDLC operation. They are generally determined using nitrogen, argon and/or CO_2 gas adsorption studies. The studies require removal of moisture from the samples via outgassing at an elevated temperature (> 150 °C) under an inert gas flow or vacuum. The sample is then cooled in liquid N_2 (77 K) (when using N_2) or a water-ice bath (273 K) (when using CO_2) while the adsorbate gas is pumped at incremental pressures into the sample-containing tube. The N_2 sorption studies in the pressure range of 10-760 Torr allows for probing the mesopores (pores > 2 nm) and the CO_2 sorption in a similar pressure range allows for probing micropores (pores < 2 nm). An isotherm is thus collected, which is a measure of the volume of gas adsorbed at a constant temperature as a function of relative pressure, the absolute pressure normalized to the condensation pressure. Using this isotherm it is possible to extract information regarding the available surface area and pore size and distribution. Figure 1.15 shows an isotherm for a mesoporous CDC.

The theory that laid the foundation for the calculations that allowed for the surface area measurements and pore structure evaluation comes from the work of Irving Langmuir. His theory assumes that the surface is homogeneous, that there is a monolayer adsorption on the surface of the studied material, and that the adsorbed molecules do not interact. The theory was further developed by Stephen Brunauer, Paul Hugh Emmet and Edward Teller (BET). Their theory applied Langmuir theory to multiple layers of

adsorption and assumed that Langmuir's theory can be applied to each layer and that each layer does not interact with the other (101).

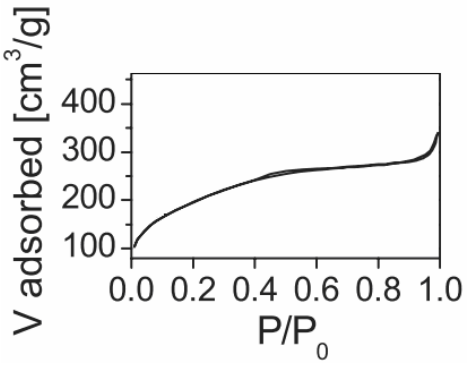

Figure 1.15. Nitrogen sorption isotherm for mesoporous SiC (102).

The BET equation (equation 1.15) can be used to find Vm, the volume of the gas necessary to form a monolayer. In equation 1.15, P is the equilibrium pressure, P_0 the saturation pressure, V_a the volume of gas adsorbed at P, A, C and I are constants. P/P_0 is the relative pressure of adsorbate. V_m can then be multiplied by N (Avogadro's number), s (the molecular cross-sectional area), and divided by V the molar volume of the adsorbent to get the total surface area. The SSA can then be obtained by dividing the surface area (obtained with equation 1.19) by the mass of the sample.

$$\frac{P}{V_a(P-P^o)} = I + A\left(\frac{P}{P^o}\right) \qquad (1.15)$$

$$I = \frac{1}{V_m C} \qquad (1.16)$$

$$A = \frac{(C-1)}{V_m C} \qquad (1.17)$$

$$V_m = \frac{1}{A+I} \qquad (1.18)$$

$$S_{BET} = \frac{V_m N s}{V} \qquad (1.19)$$

1.7.2 Raman Spectroscopy

Raman spectroscopy (RS) has been used to provide characterization of graphitic materials for the last four decades, and has been increasing in popularity significantly in the past decade due to growing interest in carbon materials. The information obtained by RS can provide insight into structure defects, graphene layer stacking, and finite size of the crystallites parallel and perpendicular to the hexagonal cell axis. The peak associated with graphite is termed the G peak, and the peaks associated with disorder of the carbon sample are D and D' (103). The peaks are the result of double-resonance occurring during the Raman process. G is the result of in-plane bond stretching motion of pairs of C sp2 bonded atoms (104). Generally, the absence of perfect graphite systems leads to the constant presence of some D band signal. These defects, however, are often desirable in graphitic materials due to the anisotropy of properties found in graphitic systems. For instance the weak van-der-walls forces found between the graphene layers can be ameliorated by having small crystals, which will increase the mechanical strength of the graphite as compared to long planes of graphene sliding past one and other.

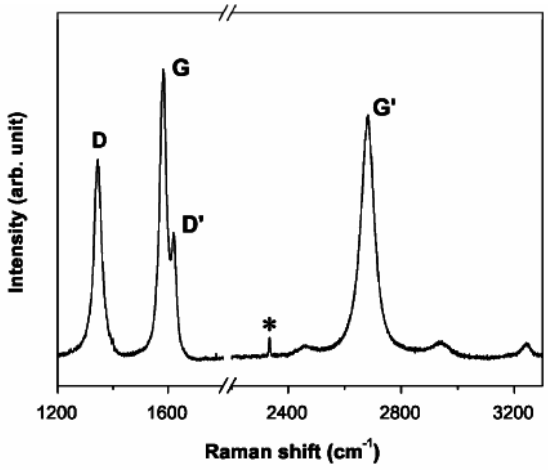

Figure 1.16. Raman spectrum of a nanographite sample, showing the main Raman features. Taken with a laser excitation wavelength of 514.5 nm. The * peak is from

nitrogen in the air and non-prominent graphite features are not labeled, but have been assigned through other investigations (103).

RS is a quick, easy, non-destructive, non-contact method for probing the structure of carbon via inelastic scattering of light from a sample surface at room temperature in ambient pressure. The most prominent features for graphitic materials are the G, D, D' and G' bands (see figure 1.16). The G (graphite) band is found at ~1582 cm^{-1}, D at ~1350 cm^{-1}, D' ~1620 cm^{-1}, and G' ~2700 cm^{-1}, the last three varying based on laser intensity. The G band is a doubly degenerate phonon mode (E_{2g} symmetry), and indicates that the sample has sp^2 carbon networks. D and D' are defect-induced Raman features, which are unseen in highly crystalline graphite. The integrated intensity ratio of the G and D bands (I_D/I_G) is used to characterize the varying amounts of defects as the material is modified. Figure 1.17 illustrates the disorder-induced character of the D band by examining the G and D band confocal images and Raman spectra. The image is of highly oriented pyrolyzed graphite deposited on a glass substrate. Figure 1.17a of the G band image shows that it is uniform throughout the crystallite. Figure 1.17b, however, shows that the D band is localized to the imperfect edges of the sample. Figure 1.17c illustrates via the spectrum graph that at a point taken away from the edge the D band is not evident and at the edge the G band maintains its intensity, but a prominent D band appears. Other information that can be obtained from the spectra includes in-plane crystallite size as shown by the work of Tuinstra and Koenig, and variation in the stacking order of the graphene sheets along the c-axis via G', the second order of the D band. As ordering along the c-axis occurs (2-D to 3-D graphite), e.g. by heat treatment, G' band splits from

one peak to multiple peaks. Other researchers further developed Tuinstra and Koenig's work and a formula to calculate crystallize size has been formulated.

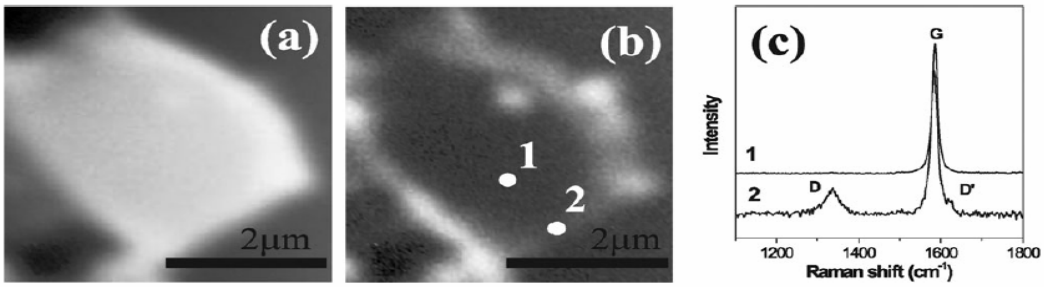

Figure 1.17. a) G band and b) D band confocal Raman images of a graphite crystallite deposited on a glass substrate. c) The Raman spectra from region 1 and 2 in panel b. Excited by a 633 nm wavelength laser (103).

1.7.3 X-ray Diffraction

X-ray diffraction (XRD) is a technique that allows for probing the crystallographic structure and chemical composition of materials. This is done by measuring the scattered intensity of x-rays coming off a sample post incidence as a function of incident and scattered angle.

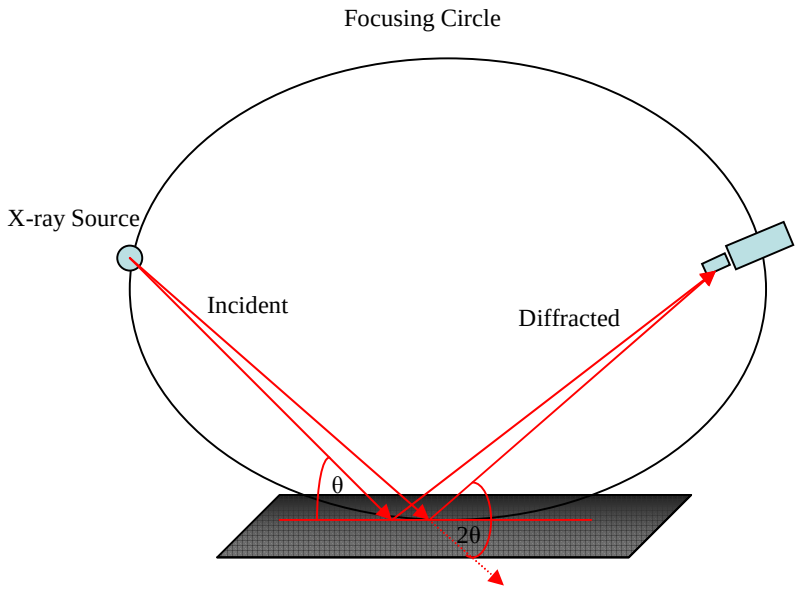

Figure 1.18. Bragg Bentono geometry for XRD structure probing.

The common configuration used for XRD is the Bragg Bentono geometry, which allows for a constant distance between the sample and the detector (figure 1.18). It essentially requires that the distance from the source to the sample and sample to detector is kept constant and that the sample is tangent to the focusing circle. In order to keep the detector distance constant the sample must rotate at 1/2 the angular velocity of the detector. As the angle of incidence (θ) changes, the detector must move 2θ. A sample resulting spectrum from such a measurement is shown in figure 1.19. As it can be seen in figure 1.19 it is rare that the detector receives a scattered signal from the sample. This is due to destructive interference taking place in the sample and constructive interference (satisfying Bragg's Law, equation 1.20) associated with crystallinity causes the appearance of peaks.

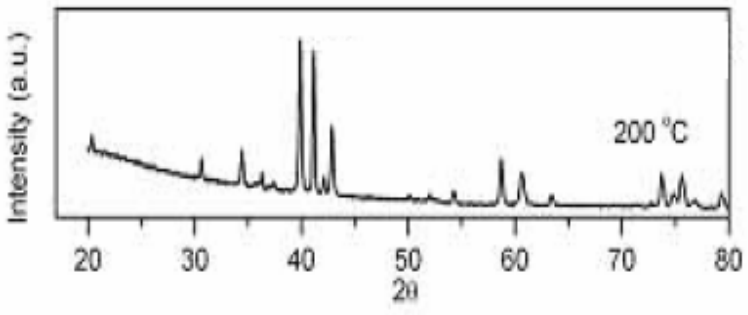

Figure 1.19. X-ray diffraction pattern of Ti_3SiC_2 CDC (85).

$$\lambda = 2d\sin\theta \qquad (1.20)$$

Where λ is the wavelength of the probing radiation, d is the feature spacing (e.g. plane spacing), and θ is the incident angle.

Small-angle X-ray scattering (SAXS) is a technique utilizing elastic scattering of X-rays, which has features in the nanometer range and is recorded at low angles (< 10°). It can provide information regarding size and shape of macromolecules, partially ordered materials, and pore sizes.

In SAXS a monochromatic beam of X-rays is brought to a sample from which X-rays scatter. A detector picks up the small portion that actually scatters, rather than goes through the material, and this pattern contains information on the structure of the sample. The experiment usually follows the procedure seen in figure 1.20.

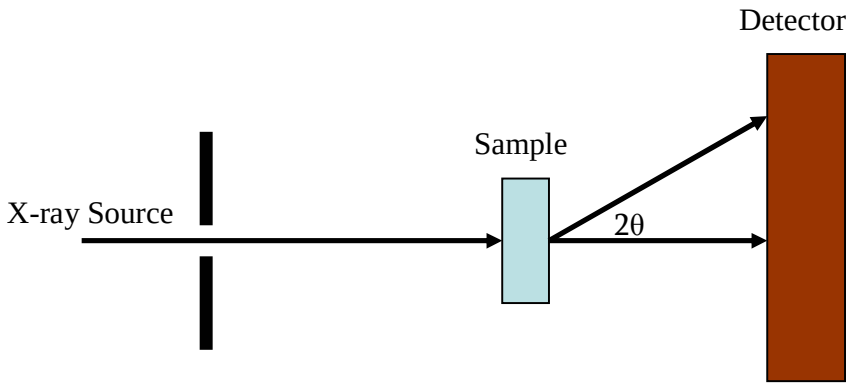

Figure 1.20. General setup for small angle x-ray scattering experiment.

1.7.4 Scanning Electron Microscopy

Scanning electron microscopy (SEM) images the surface by scanning it with a high-energy beam of electrons. The beam interacts with the surface atoms (to some small depth of up to a few microns) and produces signals that contain information about topography, composition and other possible information, such as structure. The signals emitted from the surface include secondary electrons, back scattered electrons, characteristic X-rays, and other various types of radiation. The common method of characterizing the topography is via the secondary electron imaging with up to 1 to 5 nm resolution. Typically the electron beam is created by heating a filament and then

accelerating the electrons via a potential. The beam's energy is between 40 keV and a few hundred keV and is focused by one or two condenser lenses to a spot between 0.5 and 5 nm in diameter. As the beam passes through the SEM column (figure 1.21) it is collimated with various coils or deflector plates and is then rasterized across the surface of the sample to form an image.

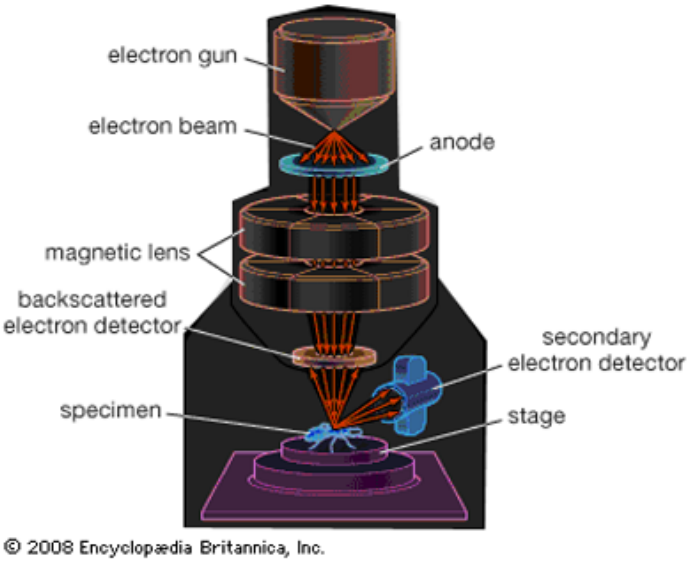

Figure 1.21. Schematic of scanning electron microscope (105).

CHAPTER 2

MATERIALS AND EXPERIMENTAL METHODS

2.1 Materials

2.1.1 Porous Carbide-Derived Carbon Formation

Mesoporous CDC were prepared by the group of Prof. Stefan Kaskel (Triebenberg Laboratory, Institute for Structure Physics, Dresden University of Technology, Dresden, Germany) using a SiC precursor having ordered mesopores. Etching of silicon from SiC was achieved via the flow of Cl_2 gas at atmospheric pressure and a temperature range of 700-1000 °C according to the following reaction (106)

$$SiC + 2Cl_2 \rightarrow SiCl_4 + C$$

The employed procedure placed 0.3 g of mesoporous SiC material into a quartz boat and slowly (8 °C/min) heated to the desired temperature under Ar flow at the rate of ~30 mL min^{-1}. At the desired temperature Cl_2 gas at the flow rate of ~30 mL min^{-1} was introduced for 3 hours. Cl_2 flow was then stopped and the sample was cooled down to room temperature under Ar flow. The samples were then brought up to 600 °C under argon and then ammonia was flowed for 2 hours to remove any excess chlorine, the samples were then cooled to room temperature under argon. The mesopores existing in SiC allowed for the successful formation of SiC CDCs at temperatures as low as 700 °C, which is not feasible when using non-porous SiC due to the high chemical stability of SiC leading to a very slow reaction rate at this temperature (82).

2.1.2 Mesoporous SiC Preparation

Mesoporous SiC was prepared using a high quality SBA-15 mesoporous SiO_2 template. According to the employed procedure (82), 2g of SBA-15 was infiltrated with 2.5 g of polycarbosilane precursor solution (Mw=800 from Aldrich) in a heptane-butanol mixture in an open beaker and left to evaporate overnight while stirring. The resulting powder was then placed in an alumina boat in a tube furnace under Ar flowing at the rate of ~ 40 mL min^{-1} and heated to 1000 °C according to the following regime: (a) heating from RT to 150 °C at the rate of 2.5 °C/min, (b) 5 h heat treatment at 150 °C, (c) heating from 150 to 700°C at the rate of 0.6 °C/min, (d) heating from 700 to 1000 °C at 2 °C/min, (e) annealing at 1000 °C for 2 hours and (f) cooling down to room temperature (82).

One sample (precursor for CA 27 CDC sample) was prepared slightly differently: (a) additional carbon was added to the SBA-15 template by infiltration of divinylbenzene in addition to the polycarbosilane (SMP-10 from Starfire), which was then annealed in a static Ar atmosphere for twelve hours at 250 °C, (b) heated under vacuum to 450 °C at ~ 1 °C/min, (c) annealed at 450 °C for 12 hours under vacuum, (d) heated from 450 to 1000 °C in Ar at ~ 1 °C/min, (e) annealed at 1000 °C for 2 hours and (f) cooled down to room temperature. The microstructure and porosity of the mesoporous SiC samples produced according to the two methods was similar (82).

In order to etch the SBA-15 template, the produced SiO_2-SiC composite was immersed into a solution of Ethanol/H_2O/40% hydrofluoric acid, shaken, and left for an hour of SiO_2 etching. Solution was then filtered over filter paper and washed with about 200 mL of ethanol for cleaning then left overnight drying in a hood and the next day the ordered mesoporous SiC CDC was collected (82).

The SBA-15 mesoporous silica template with uniform network porosity and wall thickness was prepared according to the method developed by Choi et al. using poly(ethylene oxide)-poly(propylene oxide)-poly(ethylene oxide) triblock copolymer (EO20PO70EO20) and sodium silicate aqueous solution (107). The synthesized SBA-15 is composed of two dimensional hexagonal arrays of channels that range from 5-9 nm in diameter. SBA-15 has large uniform ordered pores accompanied by smaller disordered pores that provide connectivity between adjacent large pores.

A schematic for the entire process for the formation of mesoporous CDC is illustrated in figure 2.1.

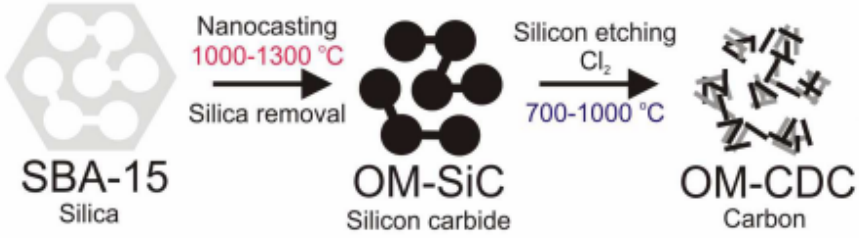

Figure 2.1. Schematic of synthesis of ordered mesoporous CDC (82) .

2.2 Electrode Preparation

The produced SiC CDC powders were suspended in ethanol and mixed with polytetrafluoroethylene (PTFE) (60 wt. % water suspension, Sigma Aldrich, USA) binder to form a slurry of 95% wt. carbon and 5% wt. PTFE. Once most of the ethanol was evaporated under continuous stirring at 300 rpm and 100 °C, the material was further mixed using a spatula until a soft clay-like consistency was achieved and the resulting composite paste was made into a thin, rubbery film, known as an electrode or peel. After drying overnight at 80 °C under vacuum the peel was rolled to the thickness of ~ 130

micron using a commercial rolling mill and left to dry in the vacuum oven at 80 °C for at least 8 hours till the EDLC device with organic electrolyte was constructed and used for electrochemical testing.

2.3 Device Assembly

The EDLCs were assembled in a symmetrical two-electrode configuration (figure 1.4). The area of the carbon electrodes was ~1 cm^2. Al foil of 300 µm in thickness was roughened using a 600 grit SiC sandpaper, coated by a thin layer (~ 10-20 µm) of a conductive paint (EB-012, Acheson Colloids, US) and used as a current collector. The conductive paint was used to reduce the interfacial resistance between the electrode and the current collector (108). A GORE^{TM} membrane (W.L. Gore and Associates, US) of ~25 µm in thickness and ~60% porosity was used as a separator for the EDLC devices. The Al-electrode-separator-electrode-Al sandwich was clamped between two Teflon slabs and transferred into the Ar-filled glovebox (Innovative technologies, <1 ppm of H_2O). After outgassing in a glovebox vacuum oven at 120 °C for two hours, the whole assembly was cooled down to room temperature and placed in a glass beaker and filled with an organic electrolyte. We selected 1 M tetraethylammonum tetrafluoroborate salt (electrochemical grade, Alfa Aesar, US) solution in acetonitrile (99.9%, extra dry, Across Organics, Geel, Belgium), the most common organic electrolyte used by the majority of the US manufacturers of commercial EDLC devices. Prior to electrolyte preparation, $TEABF_4$ salt was dried for two hours at 150 °C in a vacuum oven located inside the glovebox. The beaker-type EDLC device was placed into a custom designed air-tight glass cell equipped with two Swagelok ® electrical feedthroughs and taken out of the

glovebox for electrochemical characterization. All the electrochemical tests were performed outside the glovebox using the same Ar-filled air-tight glass cells.

2.4 Electrochemical Measurements

A powerful combination of electrochemical techniques was used to evaluate the electrode performance: cyclic voltammetry (CV), charge-discharge (C-D) tests and electrochemical impedance spectroscopy (EIS). The EIS and CV tests were carried out using a Zahner IM6 electrochemical workstation (Zahner-Elektrik Gmbh & CoGK, Kronach, Germany) in the frequency range of 1 mHz to 100 kHz with a 10mV AC amplitude. Most CV tests were performed in the voltage range of -2V to + 2V at sweep rates of 1 mV/s, 10 mV/s and 100 mV/s. Additional experiments were also performed in the range of -2.3V to +2.3V, -2.5V to +2.5V, and -2.7V to +2.7V at 100 mV/s. The C-D tests were carried out using an Arbin SCTS supercapacitor testing system (Arbin Instruments, TN, US) between 0 to + 2 V at charge (discharge) current densities between 100 and 15000 mA/g, based on the mass of a single electrode.

2.5 Gas Sorption

The isotherms of N_2 gas adsorption on the surface of CDC powders were collected at 77 K in the range of relative pressures of 0.05-1 P/P_0 using TriStar II 3020 surface area and porosity measurement system (Micromeritics Inc., GA, USA) and used for measurements of the SSA and pore size distribution (PSD) in the mesopore range (2-50 nm). CO_2 sorption tests at 273 K (ice bath) were carried out using the same system in order to measure the PSD of micropores (<2 nm). Prior to sorption tests, CDC samples (~10 mg) were degassed at 300 °C for 5 hours under continuous N_2 flow. The SSA and PSD were calculated using the BET and DFT methods, respectively. Both the BET and

DFT analyses were performed using Micromeritics software. The DFT model assumed slit pore shape. The relative pressure range of P/P_0 from 0.05 to 0.2 was used for multi-point BET calculations. Ultra high purity gases (99.99 %, Airgas, USA) were used for all experiments.

2.6 X-Ray Diffraction

X-ray diffraction studies of CDC samples were performed using a Panalytical X'Pert PRO Alpha-1 diffraction system (Pananalytical, Almelo, Netherlands) equipped with the incident beam monochromator. The system allowed to use only the $K\alpha_1$ component of Cu radiation, improving the overall quality of the collected powder diffraction data. An accelerating voltage of 45 kV, current of 40 mA, 2θ-step of 0.017, and a hold time of 200 seconds. In addition, a Nanostar (Bruker) and a Histar 2D detector was used by Krawiec et. al. to obtain the SAXS data.

2.7 Raman Spectroscopy

Micro-Raman spectroscopy was performed using an Ar ion laser excitation (488 nm) on a Ramascope 1000 Raman microspectrometer (Renishaw, UK) equipped with a charged coupled device (CCD) detector and an optical microscope for focusing the incident laser beam to a 1-2 μm spot size. The spectra were collected in the extended regime in the range of 800 - 1800 cm^{-1}. Prior to analysis, the microspectrometer was calibrated using a plain Si wafer.

2.8 Electron Microscopy

Scanning electron microscopy (SEM) was used to characterize the morphology of the CDC samples. It was performed using a LEO 1530 SEM microscope (LEO, Osaka,

Japan, now Nano Technology Systems Division of Carl Zeiss SMT, MA, USA). In-lens secondary electron detector was used for the studies, most of which were performed using an accelerating voltage of 5 kV and a working distance of 5 mm.

CHAPTER 3

ELECTROCHEMICAL CHARACTERISTICS OF SILICON CARBIDE DERIVED MESOPOROUS CARBON FILMS

3.1 Introduction

As described in Chapter 1, energy storage in EDLCs is based on the adsorption of ions under an applied potential (Figs. 1.4., 1.6). While EDLCs offer lower energy density than most rechargeable batteries, they posses higher power densities and very long cycle lives (54). Most commercial EDLCs employ activated carbon electrodes due to their high SSA, good electrochemical stability and reasonably high electronic conductivity in organic electrolytes (11). Most activated carbons exhibit relatively wide distribution of irregular curved pores in the range of 0.3-10 nm (109-111), often with narrow bottle-necks (112-114) which may dramatically slow down the ion transport and thus limit the power characteristics of EDLC (111, 114).

The wide PSD of activated carbons make the study of the effect of pore size on the ion adsorption and transport very difficult. Until recently it was believed that a pore size two-to-three times larger than the solvated ion size was appropriate to reach high capacitance values (55). Nevertheless, recent studies showed that porous carbons with subnanometer (< 1 nm) pores and a narrow PSD lead to higher capacitance values than traditional activated carbons even with a solvated ion size larger than the average pore size (58). Such a study was performed using CDC prepared from micro-sized carbide particles. CDCs are believed to have a much smaller amount of bottleneck pores than found in typical activated carbons, due to the specificity of CDC synthesis: large chloride molecules continuously exit the CDC microstructure as the chlorination progresses,

preventing pore collapse and necking (115). The CDC process also prevents uneven pore formation, which often takes place in activated carbons due to the microscopically non-uniform distribution of the oxidizing agent within the carbon being activated and (if produced from natural precursor) non-uniform carbon microstructure (116). The adverse effect of the small pores in CDC exhibiting high capacitance is that these small pores slow down the ion transport and allow for relatively moderate rate of charge (or discharge) (91, 117-119).

Many demanding applications, including power quality applications (voltage sags, most of which take place in 0.1-1 second) and pulse-power applications for the military and aerospace applications, require substantial improvements in the power characteristics of commercial EDLC, without sacrificing their energy storage characteristics. One of the potential approaches to boost the power performance of EDLCs involves minimizing the ion paths within the microporous channels of porous carbons by decreasing the size of porous carbon particles to sub-micron or, ideally, the nano-range (117). In a recent study of SiC CDC having different particle sizes (20 nm – 20 micron), Portet et al. (117) demonstrated improvements in the capacity retention with high current density and the decrease of the time constant by up to ~ 33%. As an additional benefit, decreasing the SiC CDC particle size increased its gravimetric capacitance from ~ 90-100 F/g up to ~ 130 F/g. While the study clearly demonstrated the potential for improved performance in porous carbon nanoparticles via reduction of the transport distance within each particle, the overall improvement of EDLC power characteristics was rather moderate. In addition, due to the low packing density of nanoparticles, the volumetric performance of EDLC slightly decreased.

An alternative approach to increasing the power characteristics of EDLCs may involve the use of high surface area particles, which do not posses micropores (< 2 nm). Examples of such particles include carbon nanotubes (CNT), carbon blacks, and carbon onions (50). In carbon electrodes produced from such particles ions do not need to diffuse inside long narrow channels and migrate through small bottleneck pores. However, these electrodes offer only moderately high surface areas of 200-500 m^2/g, which falls short when compared to the BET SSA of 1000-3000 m^2/g of CDCs and activated carbons, and, as a result, limited gravimetric and volumetric capacitance.

In our present study we were interested to investigate how far we could improve the capacity retention, frequency response and power characteristics of EDLC electrodes if we employed large high surface area porous carbon particles having both straight mesopore channels (for fast ion transport within each particle) and smaller pores in the volume between the large channels (for high surface area and specific capacitance). Further, we were interested to investigate how potential improvements in the power characteristics of EDLCs based on such electrodes would affect their energy storage characteristics. We selected SiC CDC produced from ordered mesoporous SiC as a material for our study (Fig. 2.1). The three samples CA28, CA 29 and CA27 were synthesized by SiC chlorination at 700, 800 and 900 °C, respectively. The details of the EDLC electrode preparation, cell assembling and testing is given in Chapter 2.

3.2 Results and Discussion: Material Characterization

3.2.1. Gas Sorption

Figure 3.1 shows the normalized N_2 and CO_2 adsorption isotherms collected at 77 K and 273 K, respectively, for all three samples. All the N_2 isotherms are of a type IV of

the Brunauer classification (120) with the volume of adsorbed N_2 increasing significantly at relative pressures above 0.1, indicating the presence of mesopores and the shape of all three CO_2 isotherms are similar. This is in contrast to CDCs previously synthesized from non-porous microscopic SiC particles, which demonstrated virtually no pores above 2 nm (121, 122). The similar shape of the isotherms suggests a very similar distribution of mesopores and micropores. It is expected that a large volume fraction of the mesopores come from the mesoporous channels existing in SiC and that the micropores are provided by the porous carbon walls. Since chlorination of SiC is known to be a conformal process (123), it is likely that the pore sizes existing in the SiC precursor would not change significantly upon SiC transformation into CDCs. The similar porosity of the three SiC precursor samples may explain the similar distribution of the volume of micro- and mesopores in the produced CDC samples.

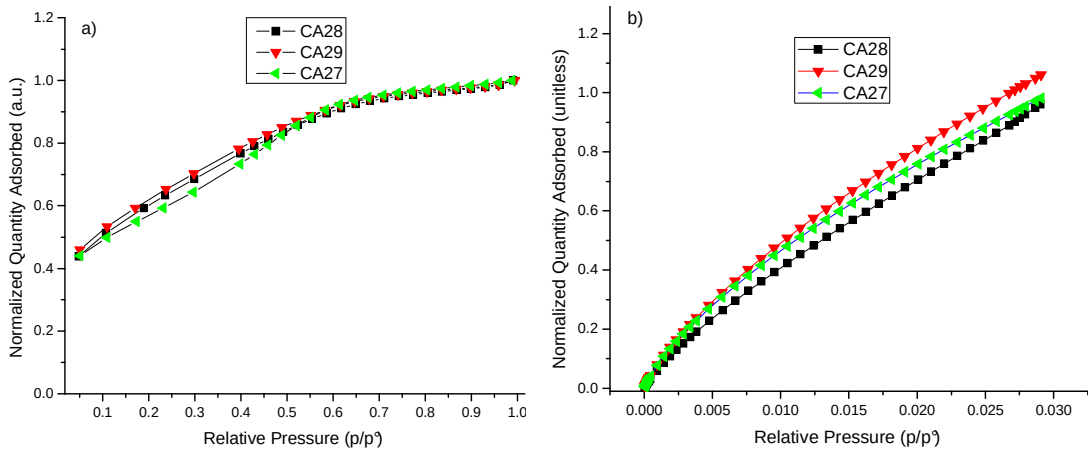

.

Figure 3.1. a)N_2 and b)CO_2 adsorption isotherms for the three CDC samples.

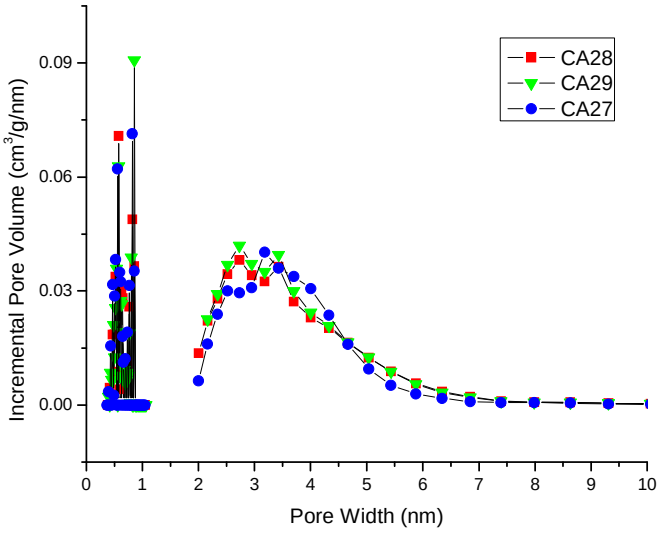

Figure 3.2. Pore size distribution of the CDC samples.

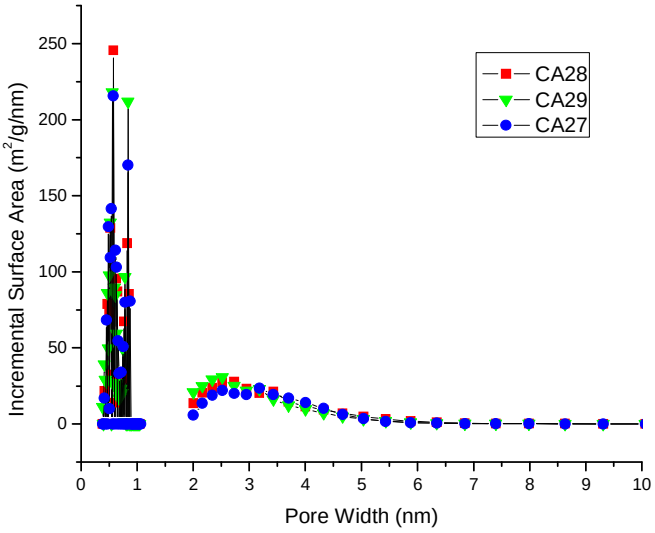

Figure 3.3. Incremental surface area distribution of the CDC samples.

The DFT PSD (Fig. 3.2) of the CDC samples demonstrated the largest volume of ~ 3 nm pores in all three samples, close to the pore size in the SiC precursor. Figure 3.3, however, demonstrated that the majority of the available surface area came from the micropore contribution. The distribution of the pores is quite similar, confirming the previous discussion. The PSD of CA28 and CA29 samples showed the strongest similarity. These samples were synthesized by chlorination of identical SiC precusors at 700 and 800 °C. On the other hand, CA27, which was produced at a higher temperature of 900 °C from the mesoporous SiC precursor was prepared slightly differently (see Chapter 2), showed a slightly different PSD of mesopores with the distribution peak shifted towards larger pores by ~ 0.5 nm. An increase in the average pore size in CDCs produced at higher chlorination temperatures has been previously observed (121, 122, 124, 125). However, SiC CDCs previously produced from non-porous SiC particles showed nearly no changes in the average pore size when the chlorination temperature was increased from 800 to 1200 °C (117, 122). As such, it might be reasonable to assume that the small deviations in the SiC precursor preparation were responsible for the larger mesopores in CA27.

The BET SSA of the samples calculated from N_2 isotherms are shown in Table 3.1. The values obtained for our SiC CDC samples (2250-2450 m^2/g) are over two times higher than those obtained for SiC CDC produced by chlorination of nonporous SiC particles at 800-1200 °C (117, 122) and among the highest reported for CDCs (124, 126) (119, 122). While chlorination of SiC nanoparticles resulted in slightly larger surface area (~ 1300 m^2/g) as compared to micrometer particles (~ 1100 m^2/g) (117), the dramatic increase in the surface area achieved by using mesoporous SiC precursor was surprising.

We speculate that the difference in SiC precursor microstructure and carbon content might be responsible for the highly developed porosity.

Table 3.1. SSA estimated by multipoint BET method.

Sample	Specific Surface Area (m^2/g)
CA28	2248
CA29	2434
CA27	2342

3.2.2. Scanning Electron Microscopy

Figure 3.4 is a low resolution SEM micrograph of the CDC electrode surface with some non-uniformities and elongated CDC particles visible. While this figure shows CA28, the other samples had a very similar appearance (not shown). Higher resolution SEM (Figs. 3.5 and 3.6) performed on all three samples revealed very similar particle morphology. Figure 3.6 demonstrates the highest magnification of all three samples, allowing for better viewing of the surface features of the particles. Because the silica membrane with elongated pores was utilized as the template for the SiC synthesis, and because during the SiC chlorination, the shape of the particles does not change significantly (127), highly elongated CDC particles were obtained, as seen in figures 3.5 and 3.6. CDC particles of up to ~ 50 micron in length (Fig. 3.4) consist of bundles of smaller carbon particles (Fig. 3.6). A CDC agglomerate consists of ~ 10 strands, having a diameter in the range of 600-700 nm. Roughly the same strand sizes were seen in the samples, though as reported by Krawiec et. al., some variation in the structural shrinkage is commonly observed during the formation of mesoporous CDC, depending on synthesis

conditions. For instance, a sample chlorinated at 700 °C resulted in a structural shrinkage of ~24%, while a sample chlorinated at 1000 °C showed ~30% shrinkage (82).

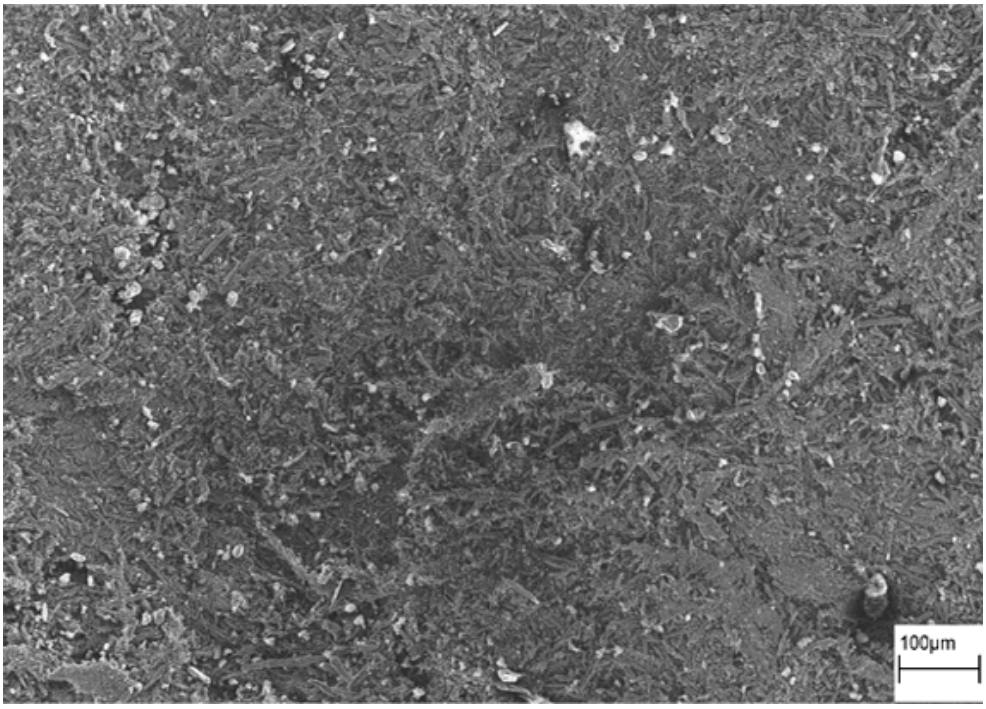

Figure 3.4. SEM of CA28 electrode film.

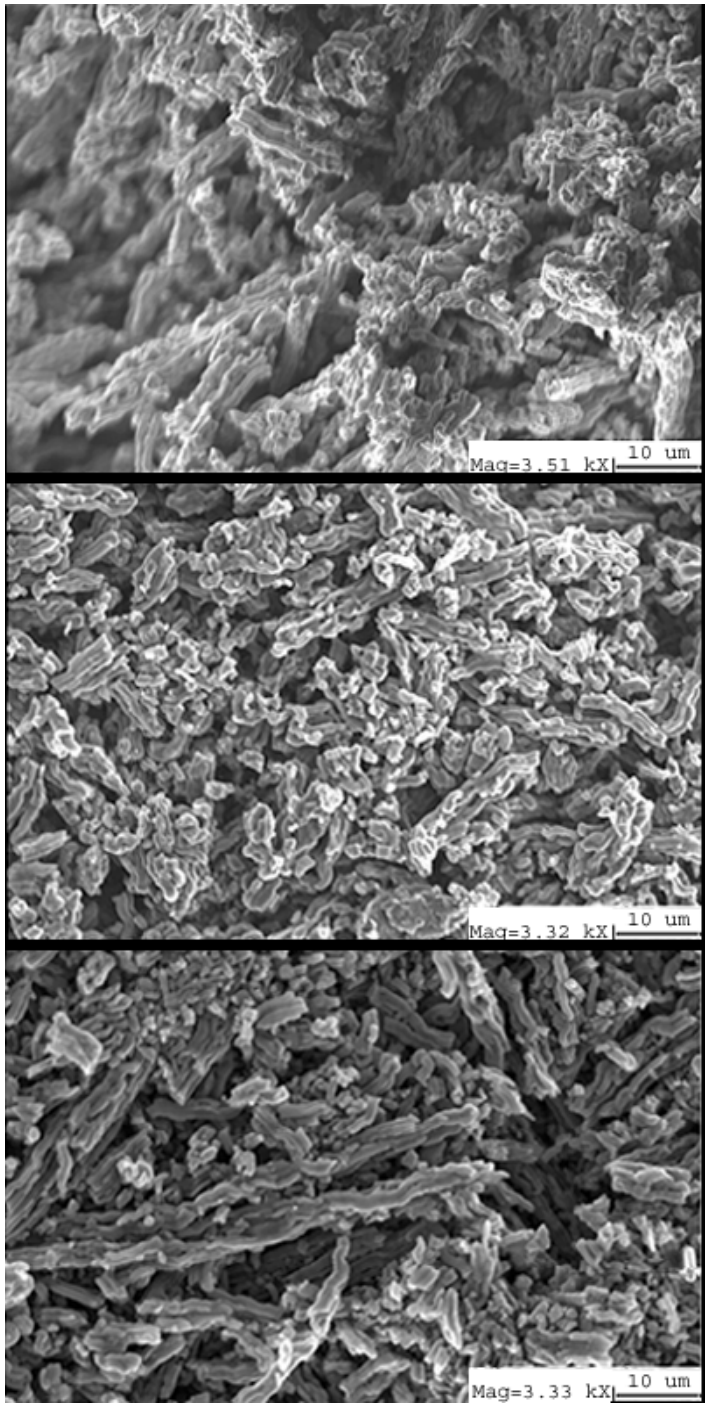

Figure 3.5. SEM of CA28, CA29, CA27 (top to bottom) electrode film.

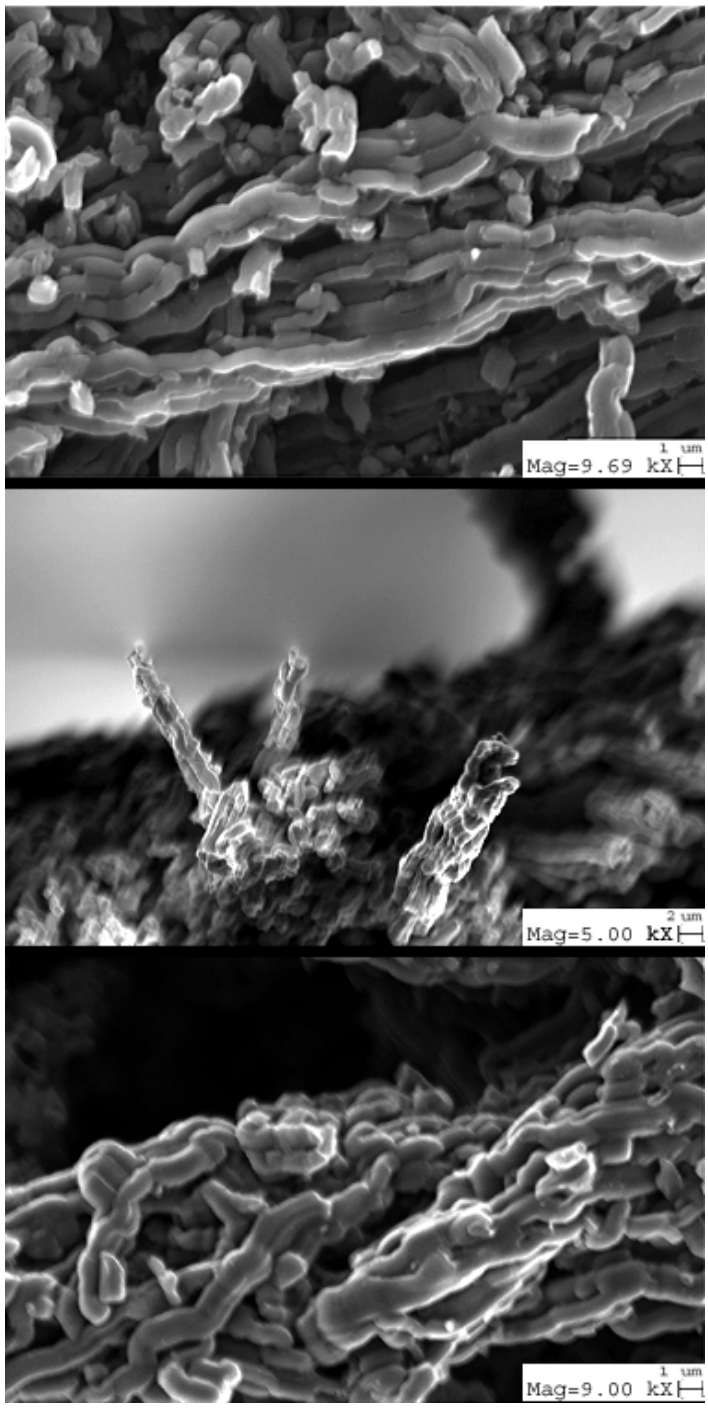

Figure 3.6. SEM of CA28, CA29, CA27 (top to bottom) electrode films at a higher magnification.

3.2.3. Raman Spectroscopy

Raman spectroscopy was used to evaluate the degree of disorder within the CDC samples. Perfect graphite shows only one Raman active mode, the G-band, located at ~1582 cm^{-1} and is independent of the excitation wavelength. This peak corresponds to graphite in-plane vibrations with E_{2g} symmetry (128, 129). Disordered carbons show an additional band at ~1350 cm^{-1} (D-band) for an excitation at wavelength λ = 488 nm (129, 130). The position of this band may vary, depending on the structure of the disordered carbon, the presence of impurities, and the excitation wavelength (130). The D-peak is associated with a double-resonance Raman process in disordered carbon. According to the double-resonance phenomenon, a phonon mode gives rise to the D-peak if the wave vector of the phonon is twice as large as the wave vector of the electronic transition in carbon excited by the incident phonon (130, 131).

Analysis of the three samples showed strong peaks corresponding to D- and G-bands (Fig. 3.7). The change in full width at half maximum (FWHM) of both the D and G bands are minimal (not shown). The ratio of integrated intensities of the D-band and G-band (I_D/I_G) decreased with increasing chlorination temperature (Fig. 3.7 b). This observation suggests that ordering increases at higher synthesis temperatures, which is consistent with previous results on CDC (121). For the I_D and I_G calculations the graphs were fitted using two Gaussian peaks corresponding to D and G bands, respectively, and the area under each peak was calculated. The peak fitting was done using Origin Pro software.

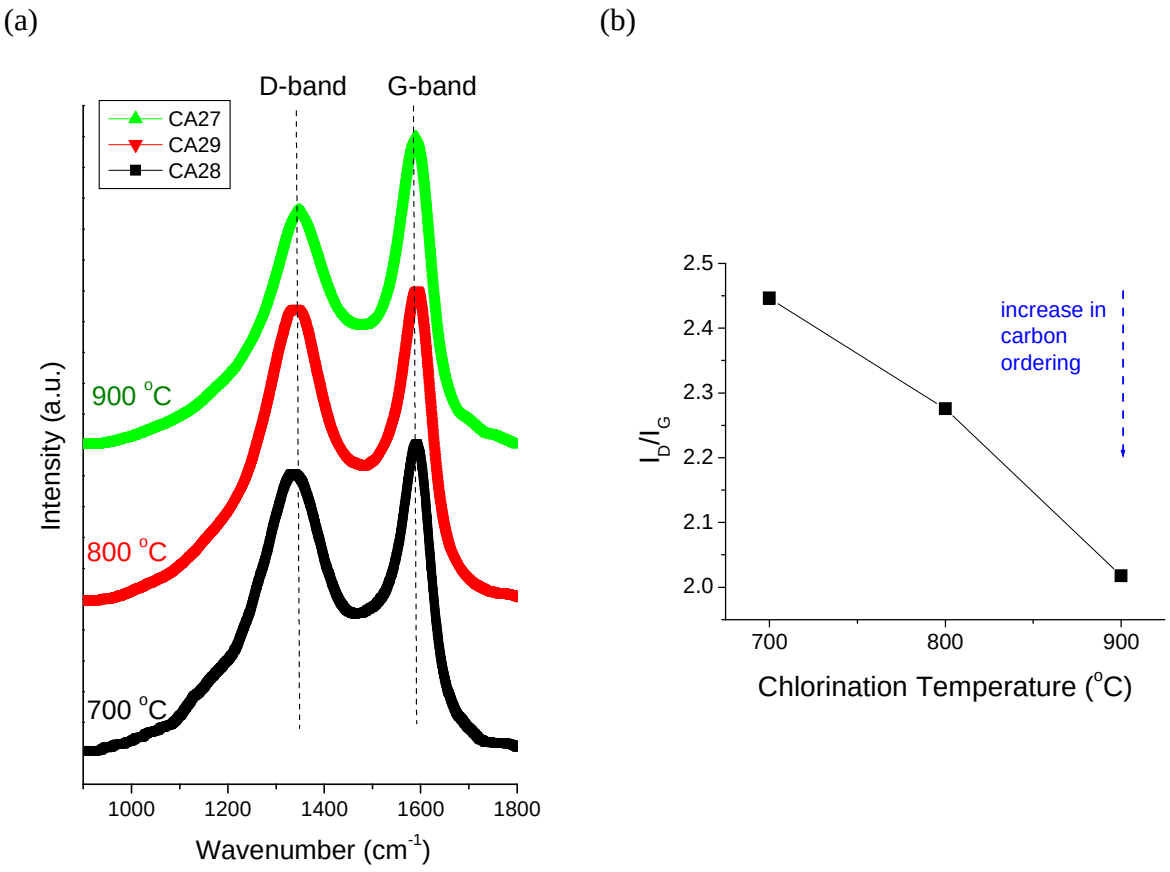

Figure 3.7. Raman spectroscopy of CDC samples: (a) Raman spectra showing the disordered structure of the samples with a prominent D-band; (b) I_D/I_G ratio as a function of chlorination temperatures

3.2.4. X-Ray Diffraction

A very weak and broad peak at ~26° (not shown) suggested extremely disordered CDC structure. In addition, a peak is not seen at ~ 44 °, which would be due to diffraction from the (101) planes of graphite, indicating the growth of graphite ribbons in CDC (132).

XRD studies at small angles were performed in order to determine if there were large features with repetitive order in the carbon samples, such as regularly spaced mesopores present in the mesoporous SiC precursor. Figure 3.8 shows that ordered large

features are found in all three samples. After analyzing the peak positions, it appears that CA27, CA28, and CA29 experienced varying amounts of shrinkage with respect to the large features (11.7%, 27.8%, and 2.2%, respectively, calculated via Bragg's Law). Surprisingly, CA29 experienced a significantly lower amount of shrinkage as compared to CA28, which was similarly prepared. Maintaining a similar pore distribution, while chlorinating at a higher temperature, which could lead to additional removal of surface passivation, and shrinking significantly less, is hard to explain. These differences require further examination, for example, via transmission electron microscopy and varying synthesis temperature to provide more insight into the phenomenon.

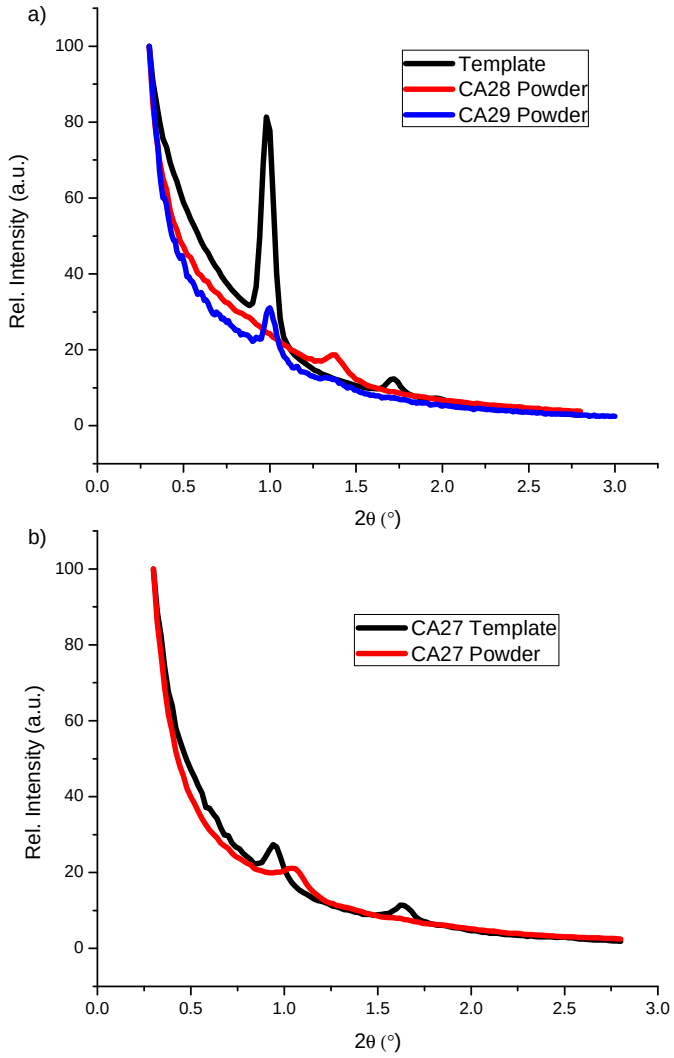

Figure 3.8. SAXS spectrums taken by Krawiec et. al. for: a) SiC precursor template, CA28 and CA29 and b) SiC precursor template and CA27

3.3 Results and Discussion: Electrochemical Characterization

3.3.1 Electrochemical Impedance Spectroscopy

EIS on the two-electrode assembled cells demonstrated high capacitance for all the mesoporous SiC CDC samples investigated, with values exceeding 140 F/g at 0.01

Hz (Fig. 3.9). This value is one of the highest values reported for porous carbons in a solution of $TEABF_4$ in acetonitrile electrolyte (100). CA28 produced at 700 °C exhibited higher specific capacitance than CA29 and CA27, both produced at higher temperatures. The capacitance of porous carbons is known to be affected by the SSA (22), pore size (118) and microstructure (50) with higher SSA, micropores and more disordered structure commonly leading to larger capacitance. The size of the micropores measured using CO_2 sorption and analyzed using DFT, as well as that of the mesopores for CA28 measured using N_2 sorption and analyzed using DFT (Fig. 3.2) was very similar to that of samples CA29 and CA27. Furthermore, the BET SSA of CA28 was only a few percent different than that of both CA29 and CA27 samples (Table 3.1). Therefore, we speculate that the more disordered microstructure of SiC CDC produced at the lowest temperature of 700 °C (Fig. 3.7) might be responsible for its excellent capacitance characteristics. Interestingly, however, the capacitance of CA29 produced at the intermediate temperature of 800 °C and exhibiting the highest BET SSA of 2434 m^2/g (Table 3.1) was the worst in the series. The mechanisms responsible for its relatively poor performance are not completely clear. In comparing CA28 and CA29 one can take into account the previously discovered phenomenon that at lower chlorination temperatures the order in the mesoporous channels of SiC precursor is easier to preserve during the CDC transformation (82). The hampered mesopore ordering may slow down the ionic transport and obviate the formation of the double layer. The better performance of CA27 as compared to CA29 sample could be due to the difference in the CA27 synthesis procedure. The DVB used in the preparation of the mesoporous SiC for CA27, to

improve the mesopore ordering (82), may result in pores that facilitate faster ionic transport.

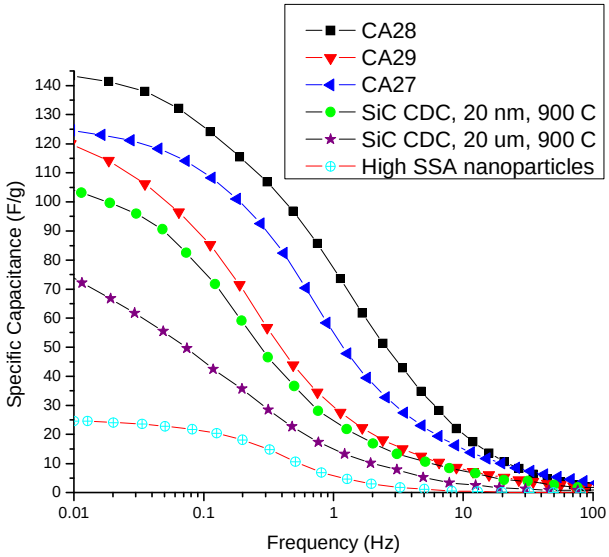

Figure 3.9. Gravimetric capacitance frequency response for investigated CDCs, contrasted with previously studied systems (50, 123).

Figure 3.9 also compares the performance of the three mesoporous SiC CDC samples with that of previously synthesized SiC CDC produced from non-porous micro- and nano-powders at 900 °C. While the performance of nano SiC CDC approaches that of CA-29, microscopic SiC CDC showed far inferior capacitance, presumably due to its lower SSA. The capacitance of that SiC CDC does not show signs of saturation at 0.01 Hz, suggesting that larger particle size and thus longer diffusion paths for electrolyte ions prevent the system from reaching the equillibrium ion adsorption within a ~100 s time period. Figure 3.9 further compares the performance of mesoporous SiC CDC with that of non-porous high surface area carbon nanoparticles, such as those produced by

annealing nanodiamond (50). As we can see they offer nearly 6 times lower specific capacitance than the SiC CDC sample CA28.

When the gravimetric capacitance is normalized with respect to the maximum capacitance for each respective system (Fig. 3.10), a comparison of the frequency response for the carbon electrodes becomes easier. CA28 clearly shows the shortest relaxation time, 50 % of its capacitance is maintained at frequencies in excess of 1 Hz. The combination of such a fast frequency response and high capacitance indicates excellent power characteristics with respect to this SiC CDC. In fact, somewhat surprisingly, both CA28 and CA27 showed better frequency response than that of non-porous carbon nanoparticles, such as annealed nanodiamond (Fig. 3.10). This could be related to the fast ionic transport in the mesoporous channels of the templated SiC CDC. In contrast, the large mesopores created by spacing between non-porous carbon nanoparticles might have a morphology, which impedes ion transport. The frequency response of CA29 was similar to that of the SiC CDC nanopowder. In order to maintain 50% of its maximum capacitance value a charge-discharge frequency of less than 0.25 Hz is needed.

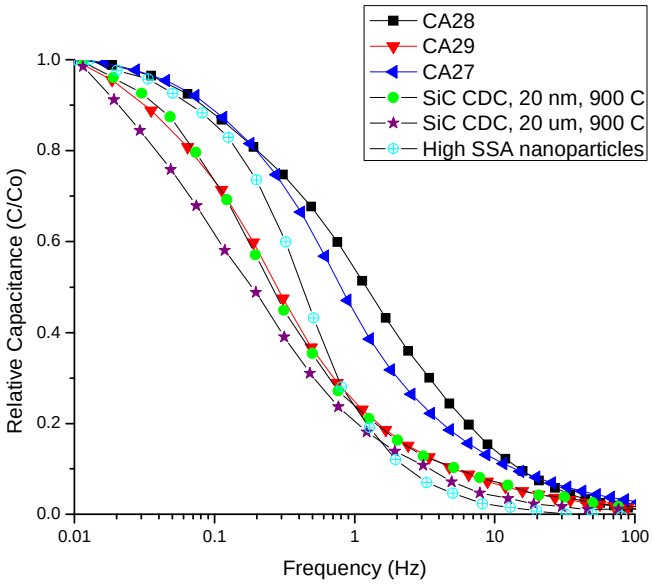

Figure 3.10. Relative capacitance vs frequency response for the investigated systems and several other materials (50, 123).

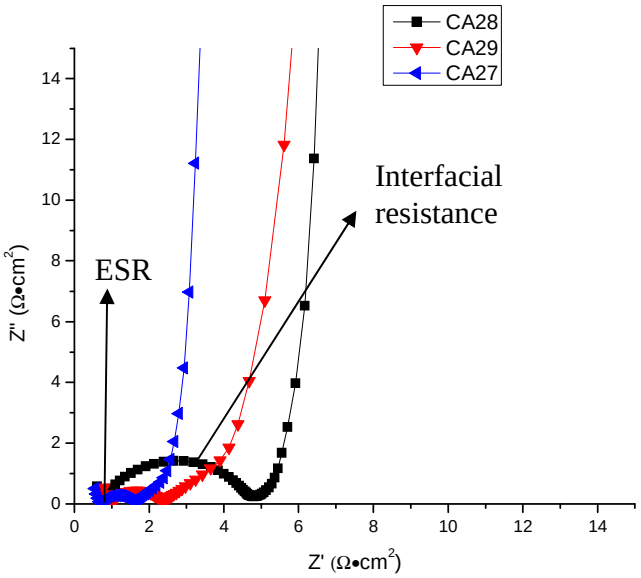

Figure 3.11. Nyquist plots for the SiC CDCs.

The Nyquist plots (Fig. 3.11) obtained by performing EIS provide some interesting insight regarding the differences in the EDLC devices based on the CA28, CA29 and CA27 CDC samples. At high frequency the capacitance of EDLC becomes

very low (Fig. 3.10) and the device operates as a resistor. It appears that the ESR values of the EDLC devices measured at high frequency are fairly similar and low, as seen in table 3.2.

Table 3.2. ESRs for the SiC CDCs.

Samples	**Equivalent Series Resistance (**Ohm·cm2)
CA28	0.76
CA29	0.98
CA27	0.72

However, the interfacial resistance between the painted Al current collectors and the SiC CDC electrodes vary more significantly. The non-ideal interface is often expressed by the appearance of the semi-circuit (R-C) loop at high frequency in the Nyquist plot (108, 133). The equivalent circuit responsible for the loop includes both the interface resistance and interface capacitance (presumably due to the surface oxide formation) in parallel to each other and in series with the the frequency-dependent capacitance and resistance of the carbon electrodes (133). A smaller interface resistance, and corresponding loop, would allow the EDLC to achieve capacitive behavior at higher frequency and minimize resistive losses during operation. The largest loop was observed in CA28, prepared at the lowest temperature, and the smallest one in CA27, prepared at the highest temperatures. This can be due to several reasons, apart from the possible differences in the thickness and uniformity of the conductive paint on the Al current collectors (as the process is not very easy to control when done by hand). Chlorine contaminants left in the samples after the high temperature treatment in ammonia may

cause corrosion of the Al current collectors and lead to the R-C loop formation. Higher content of Cl is common in CDC samples produced at lower temperatures, which may explain the shrinkage of the R-C loops upon increase in chlorination temperature (in the order of CA-28→CA-29→CA27). Furthermore, chlorination at higher temperatures often leads to lower CDC resistivity (58), which may also contribute to the R-C loop minimization.

Using Eq. 1.12 the imaginary component of the capacitance was calculated as a function of the frequency for all three samples and plotted in figure 3.12. The time constants for the devices were calculated from this graph and plotted in figure 3.13 and contrasted with that for SiC 20 nm, SiC 20 μm, and ND annealed at 1200°C particles. As the device's capacitance increases the time constant is reduced. Thus, the lower time constant for nonporous carbon nanoparticles such as ND and the two SiC particles are not surprising. Among the mesoporous SiC CDC, CA27, produced at the highest temperature, exhibited the smallest time constant. Its smaller interface resistance (Fig. 3.11), fast ionic transport, resulting in low ionic resistance (Fig. 3.10), and moderate specific capacitance (Fig. 3.9) may have contributed to achieving the observed small value of 8.6 s. The largest time constant was observed in CA29, which exhibited the highest ionic resistance (Fig. 3.10). Both CA28 and CA27 exhibited smaller time constants than TiC CDC (not shown), while having comparable specific capacitance values (59).

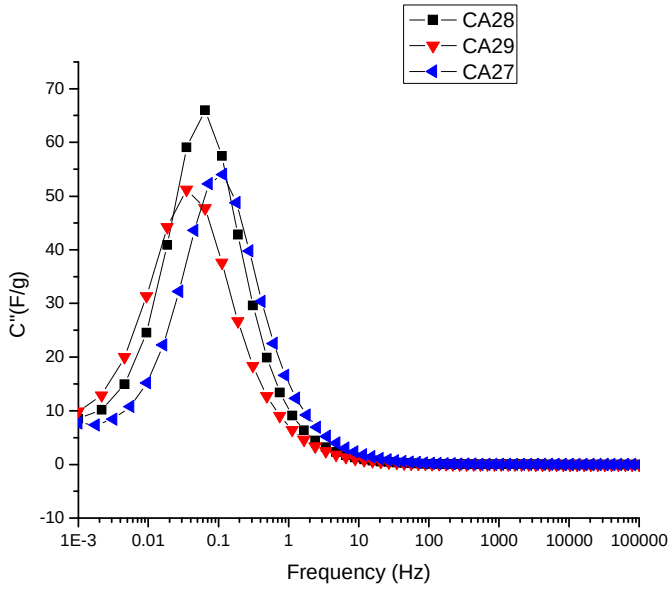

Figure 3.12. Imaginary components of the capacitance/dissipative portion of the capacitance for all three samples.

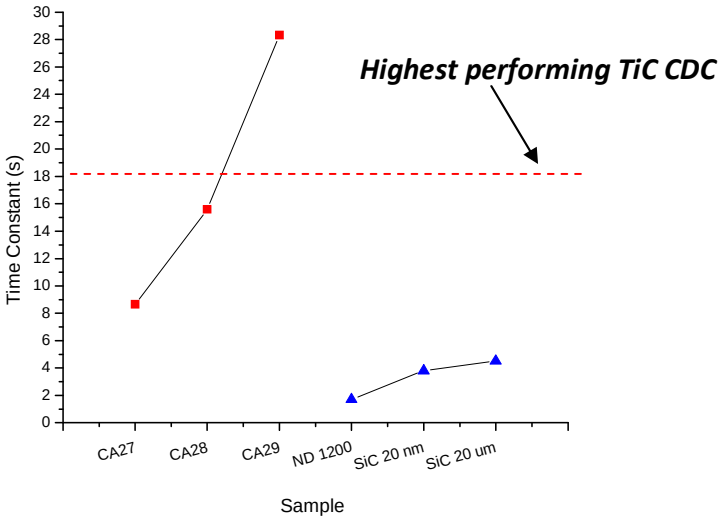

Figure 3.13. Time constants for all three samples contrasted with ND annealed at 1200 °C, and SiC particles of 20 nanometer and micrometer sizes (50, 58).

3.3.2 Galvanostatic (charge-discharge) Characterization

C-D testing is the most accepted method in industry for evaluating the gravimetric capacitance of an electrochemical capacitor, as well as the device's ability to maintain its energy storage capabilities at high discharge rates. The capacitance is calculated from the data obtained from C-D using equation 1.10. The data allowed for the calculation of the effect of current density on capacitance retention, and energy density vs. power density. Phenomenal results were obtained with respect to the absolute gravimetric capacitance obtained and the ability of the active materials to retain high energy densities even at extremely high discharge rates. The performance of the materials is contrasted with that of previously investigated SiC CDC, annealed nanodiamonds, commercial activated carbon, templated carbon, and MWNT.

The retention of capacitance at high charge and discharge rates is extremely important for power applications. Often the effect of current density (mA/g) is investigated in order to demonstrate the usability of the active material at high discharge rates. Figure 3.14 shows that the capacitance retention is excellent for the CDC investigated in this study. The data taken from previous studies show that in our particular study the current densities were much higher than often investigated, and the capacitance retention at such high rates is extremely promising for high power devices.

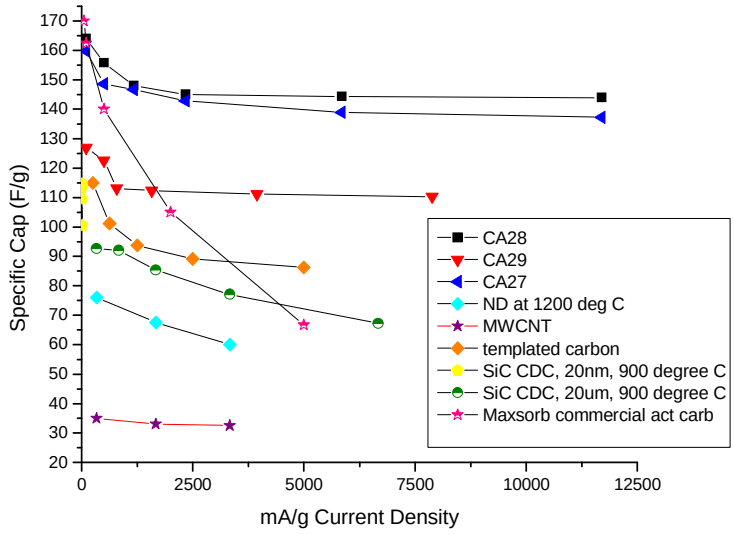

Figure 3.14. Effect of current density on gravimetric capacitance retention (50, 100, 123, 134).

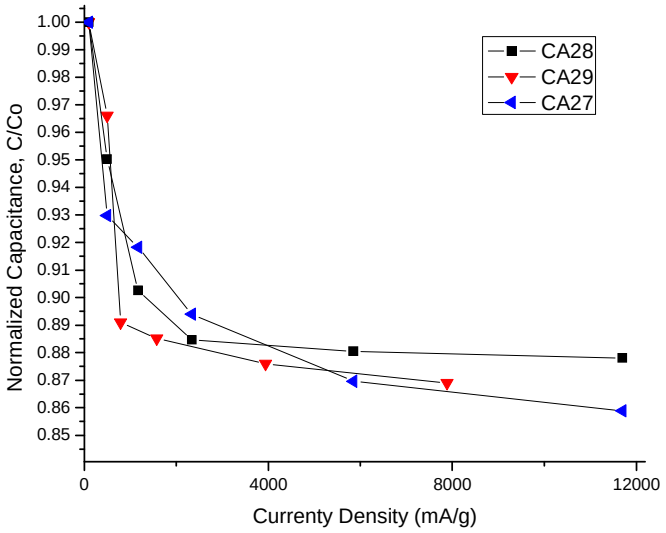

Figure 3.15. Relative capacitance retention for the samples investigated.

Figure 3.15 allows for the analyses of the relative capacitance retention for the samples studied. There is some variation at different rates of discharge, but ultimately, CA28 shows the highest retention at the highest rates. The ability of CA28 to provide the

highest capacitance, highest frequency response, and highest retention of energy storage capability at high current densities, shows some of the most promising results for applications requiring both high energy density and high power, such as hybrid electric vehicles and intermittent energy source storage applications (such as the ones necessary for solar and wind applications).

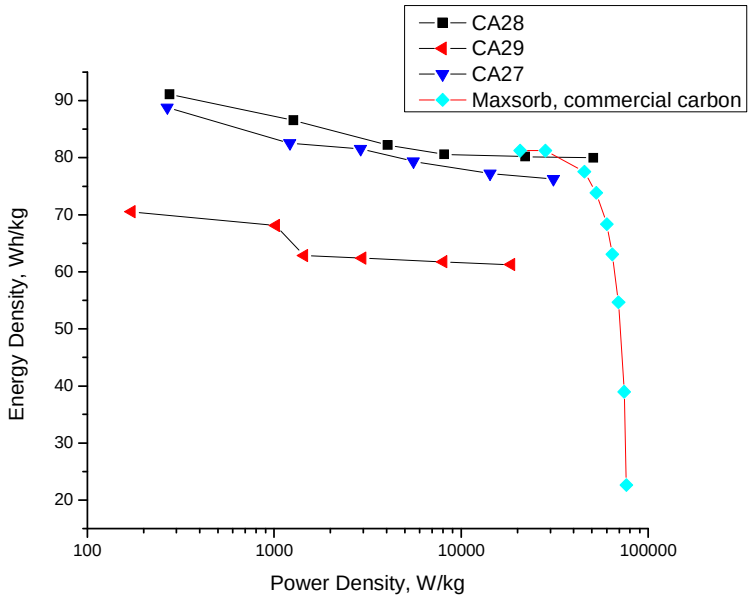

Figure 3.16. Ragone plot comparing the investigated samples and a commercial activated carbon (134).

Figure 3.16 is a Ragone plot. This plot is constructed by calculating the energy density and power density at various discharge rates. It is typical to see a great reduction in the energy density of an electrochemical capacitor as the power density is increased (by discharging faster), but it appears that in this case a superb resistance to such decay has been attained. In addition, when comparing to a commercially available activated carbon (135) the power and energy performances are shown to be very competitive.

3.3.3 Cyclic Voltammetry

CV was performed on the two-electrode cell configuration at various potential ranges and with various sweep rates. Potential ranges from -2 to +2 V, -2.3 to +2.3 V, -2.5 to +2.5 V, -2.7 to +2.7 V at 100 mV/s sweep rates were measured. The associated graphs are shown in figure 3.17-3.28 with the Y-axis being the normalized current (I/dv/dt) and specific capacitance. Table 3.3 provides the values calculated from equation 1.10 for the average gravimetric capacitance for each cycle. The tabulated data shows that capacitance is not independent of potential and that with increasing potential windows there is an increase in capacitance.

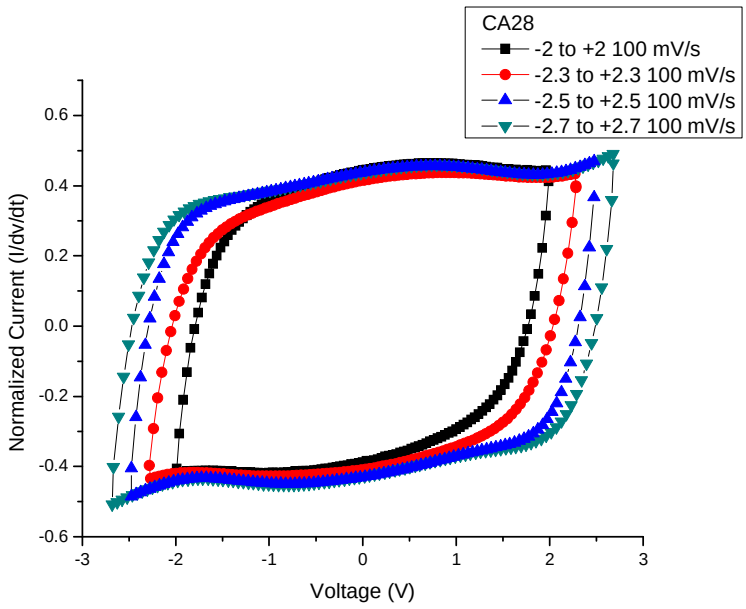

Figure 3.17. CV of CA28 at various potential ranges at 100 mV/s.

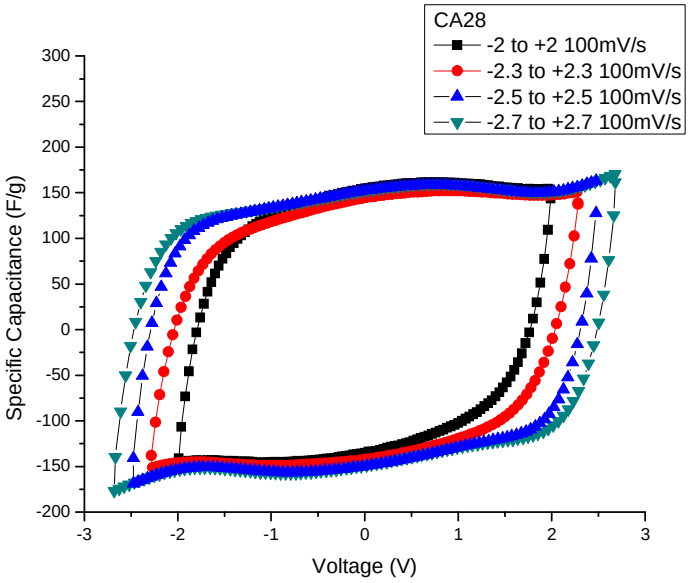

Figure 3.18. CV of CA28 at various potential ranges at 100 mV/s.

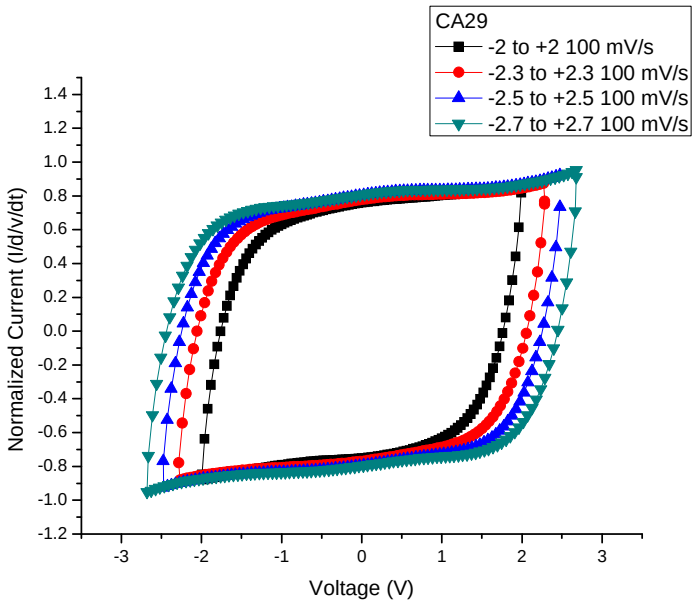

Figure 3.19. CV of CA29 at various potential ranges at 100 mV/s.

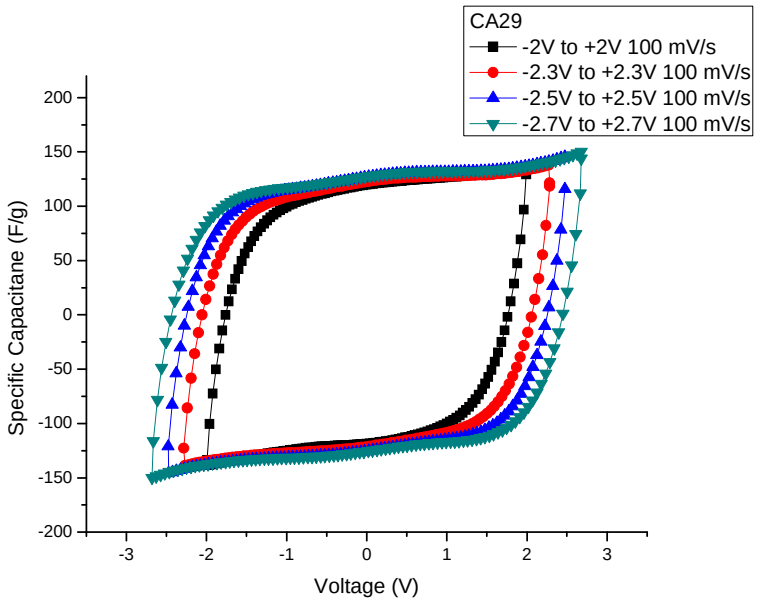

Figure 3.20. CV of CA29 at various potential ranges at 100 mV/s.

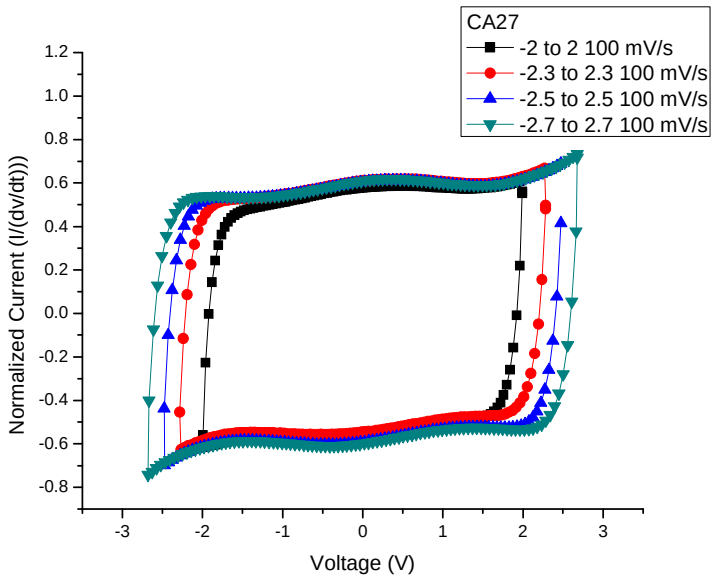

Figure 3.21. CV of CA27 at various potential ranges at 100 mV/s.

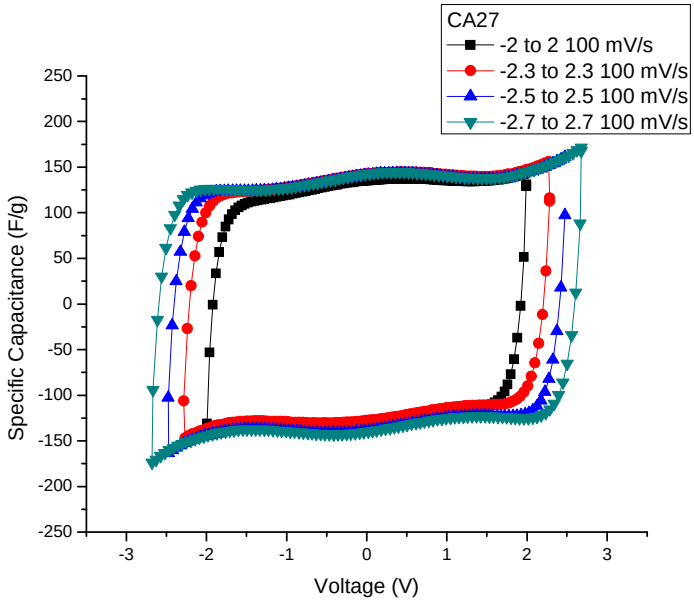

Figure 3.22. CV of CA27 at various potential ranges at 100 mV/s.

Table 3.3. Gravimetric capacitance as calculated from CV at 100 mV/s.

Sample	-2 to +2 V	-2.3 to +2.3 V	-2.5 to +2.5 V	-2.7 to +2.7 V
CA28	120.11 F/g	125.68 F/g	129.60 F/g	130.14 F/g
CA29	101.09 F/g	104.90 F/g	109.34 F/g	111.00 F/g
CA27	120.92 F/g	113.79 F/g	128.05 F/g	129.69 F/g

Cyclic voltammograms were also taken in the potential range of -2 to +2 V at sweep rates of 1, 10, and 100 mV/s. Figures 3.23-3.28 are the resulting voltammograms and table 3.4 has the tabulated values of the calculated average gravimetric capacitance from this data.

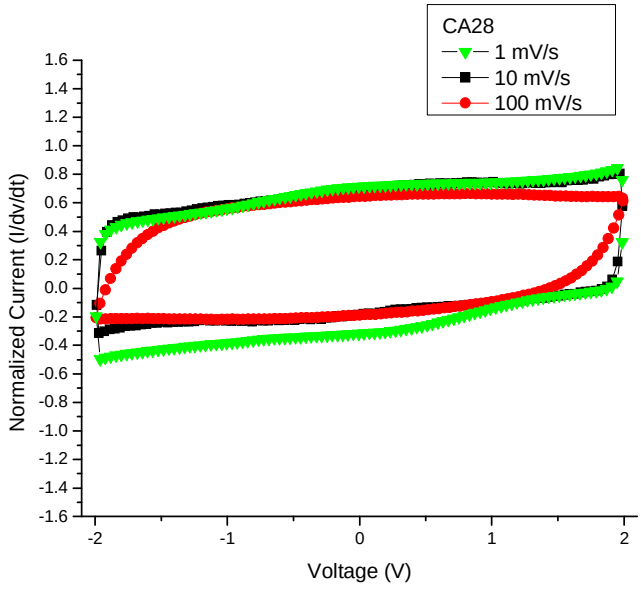

Figure 3.23. CV of CA28 from -2 to +2 V at multiple sweep rates.

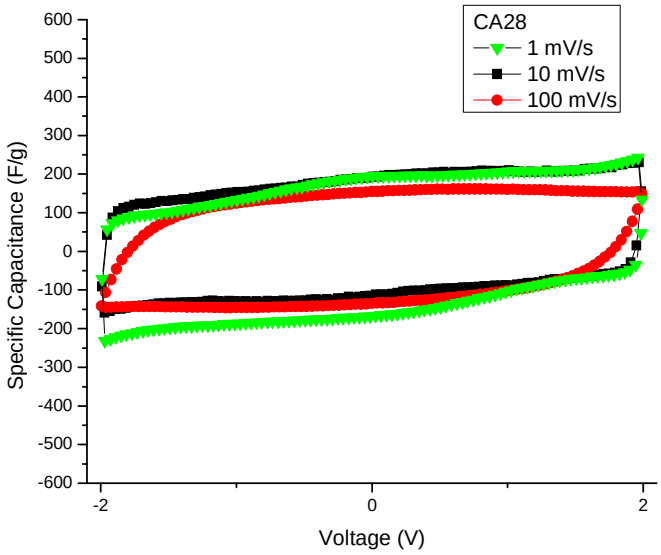

Figure 3.24. CV of CA28 from -2 to +2 V at multiple sweep rates.

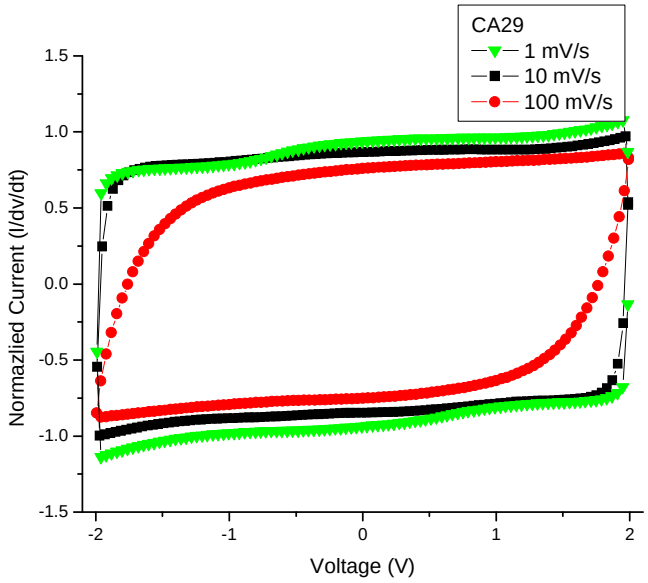

Figure 3.25. CV of CA29 from -2 to +2 V at multiple sweep rates.

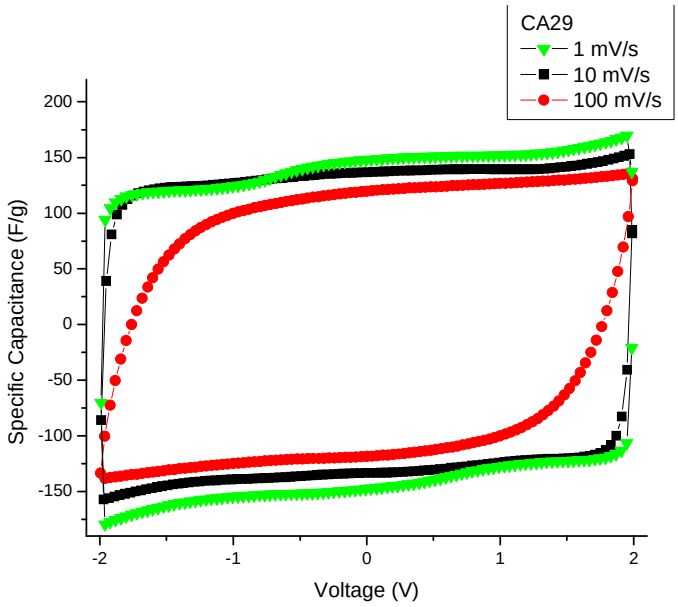

Figure 3.26. CV of CA29 from -2 to +2 V at multiple sweep rates.

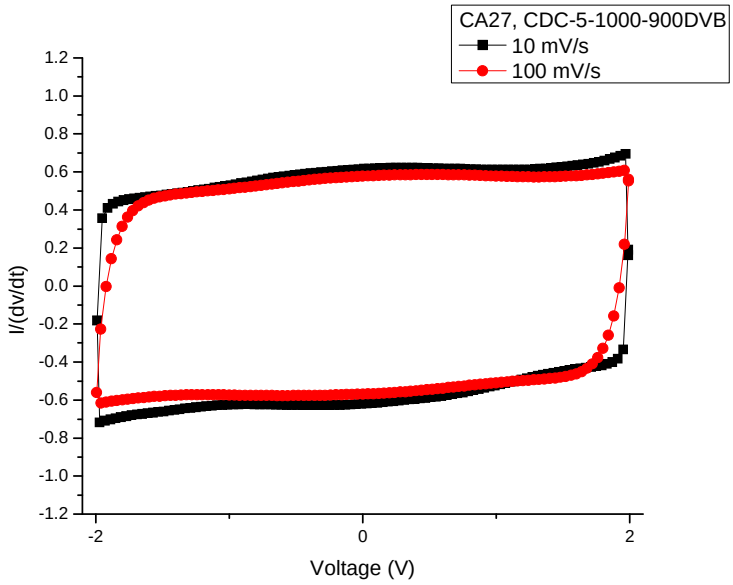

Figure 3.27. CV of CA27 from -2 to +2 V at multiple sweep rates.

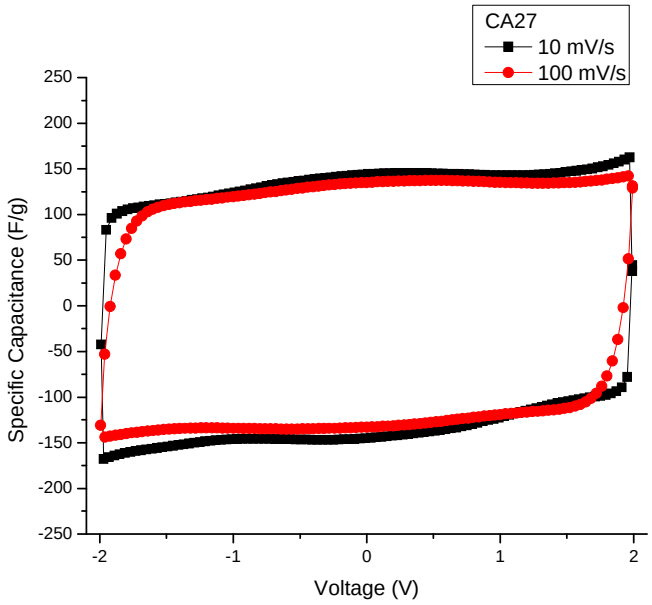

Figure 3.28. CV of CA27 from -2 to +2 V at multiple sweep rates.

Table 3.4. Gravimetric capacitance as calculated from cyclic voltammetry at various sweep rates between -2 to +2 V.

Sample	1 mV/s	10 mV/s	100 mV/s
CA28	158.62 F/g	141.43 F/g	120.11 F/g
CA29	141.29 F/g	130.94 F/g	101.09 F/g
CA27	150.80 F/g	134.29 F/g	121.07 F/g

The gravimetric capacitance found from the cyclic voltammograms follows a decreasing trend with increasing sweep rate, as commonly observed (11). The reason for this apparent loss in capacitance stems from the inability of the ions to move through the pores at fast enough rates to form the equilibrium double layer on all the available carbon surface area. The insufficiently fast ionic transport also distorts the shape of the CV curves. In addition, several voltammograms showed a distinctive slope particularly at the lowest sweep rate. This slope may result from a small leakage current. The summary of the specific capacitance data presented in Table 3.4 confirms the previously measured trends and shows the highest specific capacitance in CA28 and the smallest in CA29 samples. At the fastest sweep rate of 100 mV/s, CA27 slightly outperforms CA28 (Table 3.4).

CHAPTER 4

CONCLUSIONS AND RECOMMENDATIONS FOR FUTURE WORK

4.1 Conclusions

Electrochemical characterization of ordered mesoporous SiC CDC was performed via the two-electrode method in the form of an electrochemical capacitor cell and included the EIS, CV, and C-D techniques. The mesoporous SiC CDC samples were synthesized by the chlorination of a mesoporous SiC precursor produced via a polycarbonsilane impregnated SBA-15 ordered mesoporous silica template.

The conclusions that can be derived from the conducted studies are outlined below:

- The ordered mesoporous channels in SiC CDC serve as ion-highways and allow for very fast ionic transport into the bulk of the CDC particles, leading to an excellent frequency response and outstanding capacity retention at high current densities
- The ordered mesopores in SiC allowed for a greatly increased SSA and specific capacitance of SiC CDC, nearly doubling the previously reported values (123)
- The ordered mesoporous SiC CDC demonstrated extremely high potential for the fabrication of EDLCs with high energy and power density, reaching 51 kW/kg and 92 Wh/kg of energy density and power density in organic electrolyte, respectively
- The most attractive performance characteristics were achieved by the SiC CDC produced at the lowest chlorination temperature of 700 °C

4.2 Future Work

It might be interesting to produce and evaluate the performance of SiC CDC produced at a chlorination temperature lower than 700 °C. Investigations using variation of the wall thickness (seeing as it may have varied amongst all three samples) may provide interesting insight on the contribution of the wall thickness on ion transport. Not many studies have been done on thermal issues and efficiency and their possible effects on the microstructure and electrochemical properties, which might transpire, especially at high current densities. Another interesting investigation could entail examination of the effect of electrode thickness. It is possible that due to the varying pore structures in different CDCs, the ability to use thicker electrodes may become more feasible with different pore structures, for example the utilization of mesopores may facilitate the use of thicker electrodes due to increased transport rates. In order to further the understanding of why CA28 has the best performance characteristics and CA29 the worst it might be necessary to perform full chemical analysis of the samples and expand the structural and pore size analysis of the SiC CDC, including high resolution transmission electron microscopy (TEM), TEM tomography, and sorption measurements using gases of different dimensions. It might also be important to compare the EDLC characteristics of these materials in different organic electrolytes (having different sizes of solvation shells, ions and solvation energies), aqueous electrolytes, and ionic liquids.

Once more information is gathered and the effects of the CDC structure and porosity on EDLC performance are more clearly understood, it is possible that through manipulation of the microstructure, pore size and properties of SiC precursor and chlorination temperature further breakthroughs in performance can be obtained.

REFERENCES

1. H. Malmberg, Nanoscientific Investigations of Electrode Materials for Supercapacitors, Ph.D. Thesis, Royal Institute of Technology, Stockholm, Sweden (2007).

2. H. G. Sarmiento and E. Estrada, *IEEE Industry Applications Magazine*, **2**, 16 (1996).

3. H. G. Sarmiento and E. Estrada, *Industrial and Commercial Power Systems Technical Conference, 1994. Conference Record, Papers Presented at the 1994 Annual Meeting, 1994 IEEE*, p. 85 (1994).

4. D. Spillane, D. O' Sullivan, M. G. Egan and J. G. Hayes, *Applied Power Electronics Conference and Exposition, 2003. APEC '03. Eighteenth Annual IEEE*, p. 1111 (2003).

5. S. Zurek, Supercapacitor Chart, http://en.wikipedia.org/wiki/Supercapacitors (accessed June 25, 2009).

6. J. R. Miller and A. F. Burke, *Interface*, **17**, 53 (2008).

7. T. Robbins and J. M. Hawkins, INTELEC, International Telecommunications Energy Conference (Proceedings), Melbourne, Australia (1997).

8. H. I. Becker, Low Voltage Electrolytic Capacitor, U.S. Patent 2,800,616 (1975).

9. R. A. Rightmire, Electrical Energy Storage Apparatus, U.S. Patent 3,288,641 (1966).

10. S. Trasatti and G. Buzzanca, *Journal of Electroanalytical Chemistry*, **29**, A1 (1971).

11. B. E. Conway, *Electrochemical supercapacitors : scientific fundamentals and technological applications*, Plenum Press, New York (1999).

12. M. J. Sparnaay, *The Electrical Double Layer*, Pergamon Press, Oxford (1972).

13. C. M. Garner, G. Kloster, G. Atwood, L. Mosley and A. C. Palanduz, American Vacuum Society 5th International Conference on Microelectronics and Interfaces, p. 919 (2005).

14. Wikimedia Commons, Capacitor Illustration, http://en.wikipedia.org/wiki/File:Capacitor_schematic_with_dielectric.svg (accessed May 4, 2009)

15. Electrochemistry Encyclopedia 2006, Dielectric Frequency Response, http://electrochem.cwru.edu/encycl/art-d01-dielectrics.htm (accessed May 4, 2009).

16. W. D. Kingery, *Introduction to ceramics*, Wiley, New York (1976).

17. M. a. T. Endo, T and Kim, Y. J. and Ishii, K., *Carbon Science*, **1**, 117 (2001).

18. G. L. Bullard, H. B. Sierra-Alcazar, H. L. Lee and J. L. Morris, *IEEE Transactions on Magnetics*, **25**, 102 (1989).

19. N. A. Choudhury, A. K. Shukla, S. Sampath and S. Pitchumani, *Journal of the Electrochemical Society*, **153**, A614 (2006).

20. A. Burke, *Journal of Power Sources*, **91**, 37 (2000).

21. P. Simon and A. Burke, *Interface*, **17**, 38 (2008).

22. E. Frackowiak and F. Beguin, *Carbon*, **39**, 937 (2001).

23. L. Ionix Power Systems, Electrochemical Capacitors, http://www.ionixpower.com/electrochemical_capacitors.htm, (accessed May 4, 2009).

24. P. P. Barker, *Power Engineering Society Summer Meeting, 2002 IEEE*, p. 316 (2002).

25. J. A. Banner and C. S. Winchester, Proceedings of the Intersociety Energy Conversion Engineering Conference, Washington, DC, USA, p. 1168 (1996).

26. H. HelmHoltz, *Annalen der Physik*, **89**, 211 (1853).

27. G. Gouy, *Annals of Physics*, **7**, 129 (1917).

28. D. L. Chapman, *Philosophy Magazine*, **25**, 475 (1913).

29. O. Stern, *Zeit Elektrochem*, **30**, 508 (1924).

30. D. C. Grahame, *Chemical Reviews*, **41**, 441 (1947).

31. X. W. Huang, Z. W. Xie, X. Q. He, H. Z. Sun, C. Y. Tong and D. M. Xie, ICSM 2002 International Conference on Science and Technology of Synthetic Metals, Shanghai, China, **135-136**, p. 235 (2003).

32. W. M. Qiao, Y. Korai, I. Mochida, Y. Hori and T. Maeda, *Carbon*, **40**, 351 (2002).

33. J. S. Im, S. W. Woo, M. J. Jung and Y. S. Lee, *Journal of Colloid and Interface Science*, **327**, 115 (2008).

34. P. X. Han, C. Y. Wang, Z. Q. Shi, J. H. Lu, J. Qin and G. F. Yao, *Journal of Inorganic Materials*, **22**, 1046 (2007).

35. W. M. Qiao, S. H. Yoon and I. Mochida, *Energy & Fuels*, **20**, 1680 (2006).

36. Y. D. He, H. B. Liu and H. B. Zhang, *New Carbon Materials*, **17**, 18 (2002).

37. X. H. Zeng, D. C. Wua, R. M. Fu and H. J. Lai, *Materials Chemistry and Physics*, **112**, 1074 (2008).

38. C. X. Zhang, D. H. Long, B. L. Xing, W. M. Qiao, R. Zhang, L. Zhan, X. Y. Liang and L. C. Ling, *Electrochemistry Communications*, **10**, 1809 (2008).

39. W. B. Xing, J. S. Xue, T. Zheng, A. Gibaud and J. R. Dahn, *Journal of the Electrochemical Society*, **143**, 3482 (1996).

40. G. T. K. Fey, K. L. Chen and Y. C. Chang, *Materials Chemistry and Physics*, **76**, 1 (2002).

41. G. T. K. Fey, D. C. Lee, Y. Y. Lin and T. P. Kumar, *Synthetic Metals*, **139**, 71 (2003).

42. Q. Y. Li, H. Q. Wang, Q. F. Dai, J. H. Yang and Y. L. Zhong, *Solid State Ionics*, **179**, 269 (2008).

43. V. V. N. Obreja, E-MRS 2007 Symposia L and M: Electron Transport in Low-Dimensional Carbon Structures and Science and Technology of Nanotubes and Nanowires, Strasbourg , France, p. 2596 (2008).

44. Z. X. Yang, Y. D. Xia and R. Mokaya, *Journal of the American Chemical Society*, **129**, 1673 (2007).

45. M. Sevilla, S. Alvarez, T. A. Centeno, A. B. Fuertes and F. Stoeckli, *Electrochimica Acta*, **52**, 3207 (2007).

46. C. Vix-Guterl, S. Saadallah, K. Jurewicz, E. Frackowiak, M. Reda, J. Parmentier, J. Patarin and F. Beguin, *Materials Science and Engineering B*, **108**, 1-2, 148 (2004).

47. A. B. Fuertes, F. Pico and J. M. Rojo, *Journal of Power Sources*, **133**, 329 (2004).

48. I. H. Kim, J. H. Kim, B. W. Cho and K. B. Kim, *Journal of the Electrochemical Society*, **153**, A1451 (2006).

49. W. C. Fang, *Journal of Physical Chemistry C*, **112**, 11552 (2008).

50. C. Portet, G. Yushin and Y. Gogotsi, *Carbon*, **45**, 2511 (2007).

51. V. V. Panic, R. M. Stevanovic, V. M. Jovanovic and A. B. Dekanski, *Journal of Power Sources*, **181**, 1, 186 (2008).

52. S. L. Kuo and N. L. Wu, *Journal of Power Sources*, **162**, 1437 (2006).

53. T. Osaka, X. J. Liu and M. Nojima, *Journal of Power Sources*, **74**, 122 (1998).

54. K. Naoi and P. Simon, *Interface*, **17**, 34 (2008).

55. G. Salitra, A. Soffer, L. Eliad, Y. Cohen and D. Aurbach, *Journal of the Electrochemical Society*, **147**, 2486 (2000).

56. M. Endo, T. Maeda, T. Takeda, Y. J. Kim, K. Koshiba, H. Hara and M. S. Dresselhaus, *Journal of the Electrochemical Society*, **148**, A910 (2001).

57. E. Raymundo-Piñero, K. Kierzek, J. Machnikowski and F. Béguin, *Carbon*, **44**, 2498 (2006).

58. J. Chmiola, G. Yushin, Y. Gogotsi, C. Portet, P. Simon and P. L. Taberna, *Science*, **313**, 1760 (2006).

59. Z. X. Ma, T. Kyotani and A. Tomita, *Chemical Communications*, **2000**, 2365 (2000).

60. S. C. Pang, M. A. Anderson and T. W. Chapman, *Journal of the Electrochemical Society*, **147**, 444 (2000).

61. J. P. Zheng, P. J. Cygan and T. R. Jow, *Journal of the Electrochemical Society*, **142**, 2699 (1995).

62. J. W. Long, K. E. Swider, C. I. Merzbacher and D. R. Rolison, *Langmuir*, **15**, 3, 780 (1999).

63. A. Chu and P. Braatz, *Journal of Power Sources*, **112**, 236 (2002).

64. A. A. F. Grupioni, E. Arashiro and T. A. F. Lassali, *Electrochimica Acta*, **48**, 407 (2002).

65. M. Wohlfahrt-Mehrens, J. Schenk, P. M. Wilde, E. Abdelmula, P. Axmann and J. Garche, *Journal of Power Sources*, **105**, 2, 182 (2002).

66. J. P. Zheng and T. R. Jow, *Journal of the Electrochemical Society*, **142**, L6 (1995).

67. S.-E. Chun, S.-I. Pyun and G.-J. Lee, *Electrochimica Acta*, **51**, 6479 (2006).

68. P. Sivaraman, S. K. Rath, V. R. Hande, A. P. Thakur, M. Patri and A. B. Samui, *Synthetic Metals*, **156**, 1057 (2006).

69. J. H. Park and O. O. Park, *Journal of Power Sources*, **111**, 185 (2002).

70. K. H. An, K. K. Jeon, J. K. Heo, S. C. Lim, D. J. Bae and Y. H. Lee, *Journal of the Electrochemical Society*, **149**, A1058 (2002).

71. M. Hughes, G. Z. Chen, M. S. P. Shaffer, D. J. Fray and A. H. Windle, *Chemistry of Materials*, **14**, 1610 (2002).

72. C. F. Zhou, S. Kumar, C. D. Doyle and J. M. Tour, *Chemistry of Materials*, **17**, 1997 (2005).

73. L. Bonnefoi, P. Simon, J. F. Fauvarque, C. Sarrazin, J. F. Sarrau and P. Lailler, *Journal of Power Sources*, **83**, 162 (1999).

74. J. P. Zheng and Z. N. Jiang, *Journal of Power Sources*, **156**, 748 (2006).

75. A. Lewandowski, M. Zajder, E. Frackowiak and F. Beguin, *Electrochimica Acta*, **46**, 2777 (2001).

76. X. J. Liu and T. Osaka, *Journal of the Electrochemical Society*, **143**, 3982 (1996).

77. P. Simon and Y. Gogotsi, *Nature Materials*, **7**, 845 (2008).

78. E. N. Hoffman, G. Yushin, B. G. Wendler, M. W. Barsoum and Y. Gogotsi, *Materials Chemistry and Physics*, **112**, 587 (2008).

79. K. Vyshnyakova, G. Yushin, L. Pereselentseva and Y. Gogotsi, *International Journal of Applied Ceramic Technology*, **3**, 485 (2006).

80. Y. Gogotsi, R. K. Dash, G. Yushin, T. Yildirim, G. Laudisio and J. E. Fischer, *Journal of the American Chemical Society*, **127**, 16006 (2005).

81. G. Yushin, E. N. Hoffman, M. W. Barsoum, Y. Gogotsi, C. A. Howell, S. R. Sandeman, G. J. Phlllips, A. W. Lloyd and S. V. Mikhalovsky, *Biomaterials*, **27**, 5755 (2006).

82. P. Krawiec, E. Kockrick, L. Borchardt, D. Geiger, A. Corma and S. Kaskel, *Journal of Physical Chemistry C*, **113**, 7755 (2009).

83. R. Dash, J. Chmiola, G. Yushin, Y. Gogotsi, G. Laudisio, J. Singer, J. Fischer and S. Kucheyev, *Carbon*, **44**, 2489 (2006).

84. Y. Gogotsi, *Nanomaterials handbook*, CRC Press, Boca Raton, FL (2006).

85. E. N. Hoffman, Carbide Derived Carbon from MAX-Phases and their Separation Applications, Ph.D. Thesis, Drexel University, Philadelphia, PA (2006).

86. Z. G. Cambaz, G. N. Yushin, Y. Gogotsi, K. L. Vyshnyakova and L. N. Pereselentseva, *Journal of the American Ceramic Society*, **89**, 509 (2006).

87. S. Welz, M. J. McNallan and Y. Gogotsi, *Journal of Materials Processing* Technology, **179**, 1-3, 11 (2006).

88. J. Leis, M. Arulepp, A. Kuura, M. Latt and E. Lust, *Carbon*, **44**, 2122 (2006).

89. J. Leis, A. Perkson, M. Arulepp, M. Kaarik and G. Svensson, *Carbon*, **39**, 2043 (2001).

90. R. K. Dash, G. Yushin and Y. Gogotsi, *Microporous and Mesoporous Materials*, **86**, 50 (2005).

91. J. Chmiola, G. Yushin, R. Dash and Y. Gogotsi, *Journal of Power Sources*, **158**, 765 (2006).

92. J. Chmiola, G. Yushin, R. K. Dash, E. N. Hoffman, J. E. Fischer, M. W. Barsoum and Y. Gogotsi, *Electrochemical and Solid State Letters*, **8**, A357 (2005).

93. E. N. Hoffman, G. Yushin, M. W. Barsoum and Y. Gogotsi, *Chemistry of Materials*, **17**, 2317 (2005).

94. G. N. Yushin, E. N. Hoffman, A. Nikitin, H. H. Ye, M. W. Barsoum and Y. Gogotsi, *Carbon*, **43**, 2075 (2005).

95. E. N. Hoffman, G. Yushin, T. El-Raghy, Y. Gogotsi and M. W. Barsoum, *Microporous and Mesoporous Materials*, **112**, 526 (2008).

96. Y. G. Gogotsi, I. D. Jeon and M. J. McNallan, *Journal of Materials Chemistry*, **7**, 1841 (1997).

97. D. Avila-Brande, E. Urones-Garrote, N. A. Katcho, E. Lomba, A. Gomez-Herrero, A. R. Landa-Canovas and L. C. Otero-Diaz, *Micron*, **38**, 335 (2007).

98. R. K. Dash, A. Nikitin and Y. Gogotsi, *Microporous and Mesoporous Materials*, **72**, 203 (2004).

99. R. Kotz, M. Hahn and R. Gallay, *Journal of Power Sources*, **154**, 2, 550 (2006).

100. C. Portet, Z. Yang, Y. Korenblit, Y. Gogotsi, R. Mokaya and G. Yushin, *Journal of the Electrochemical Society*, **156**, A1 (2009).

101. S. Brunauer, P. H. Emmett and E. Teller, *Journal of the American Chemical Society*, **60**, 309 (1938).

102. Y. F. Shi, Y. Meng, D. H. Chen, S. J. Cheng, P. Chen, T. F. Yang, Y. Wan and D. Y. Zhao, *Advanced Functional Materials*, **16**, 561 (2006).

103. M. A. Pimenta, G. Dresselhaus, M. S. Dresselhaus, L. G. Cancado, A. Jorio and R. Saito, *Physical Chemistry Chemical Physics*, **9**, 1276 (2007).

104. S. Urbonaite, L. Halldahl and G. Svensson, *Carbon*, **46**, 1942 (2008).

105. Encyclopedia Britannica, Inc.,Scanning Electron Microscope, http://www.britannica.com/EBchecked/topic-art/526571/110970/Scanning-electron-microscope (accessed July 5, 2009).

106. Y. Gogotsi, A. Nikitin, H. H. Ye, W. Zhou, J. E. Fischer, Y. Bo, H. C. Foley and M. W. Barsoum, *Nature Materials*, **2**, 591 (2003).

107. M. Choi, W. Heo, F. Kleitz and R. Ryoo, *Chemical Communications*, **12**, 1340 (2003).

108. C. Portet, P. L. Taberna, P. Simon and E. Flahaut, *Journal of the Electrochemical Society*, **153**, A649 (2006).

109. S. Biniak, G. Szymanski, J. Siedlewski and A. Swiatkowski, *Carbon*, **35**, 1799 (1997).

110. K. Kaneko, C. Ishii, M. Ruike and H. Kuwabara, *Carbon*, **30**, 1075 (1992).

111. H. Shi, *Electrochimica Acta*, **41**, 1633 (1996).

112. S. M. Saufi and A. F. Ismail, *Carbon*, **42**, 241 (2004).

113. Z. Y. Yuan and B. L. Su, *Journal of Material Chemistry*, **16** ,663 (2006).

114. X. G. Zhuang, Y. S. Yang, Y. J. Ji, D. P. Yang and Z. Y. Tang, *Acta Physico-Chimica Sinica*, **19**, 689 (2003).

115. G. Yushin, A. Nikitin and Y. Gogotsi, *Nanomaterials Handbook*, CRC Press, Boca Raton, Florida, 239 (2006).

116. A. G. Pandolfo and A. F. Hollenkamp, *Journal of Power Sources*, **157**, 11 (2006).

117. C. Portet, G. Yushin and Y. Gogotsi, *J. Electrochem. Soc*, **155 (7)** (2008).

118. J. Chmiola, G. Yushin, Y. Gogotsi, C. Portet and P. Simon, *Science*, **313**, 1760 (2006).

119. J. Chmiola, G. Yushin, R. K. Dash, E. N. Hoffman, J. E. Fischer, M. W. Barsoum and Y. Gogotsi, *Electrochemical and Solid State Communications*, **8** A357 (2005).

120. S. J. Gregg, *Adsorption, surface area, and porosity*, Academic Press, London, England (1982).

121. G. Yushin, Y. Gogotsi and A. Nikitin, *Nanomaterials Handbook*, CRC Press, 237 (2006).

122. G. Yushin, R. K. Dash, Y. Gogotsi, J. Jagiello and J. E. Fischer, *Advanced Functional Materials*, **16**, 2288 (2006).

123. C. Portet, G. Yushin and Y. Gogotsi, *Journal of the Electrochemical Society*, **155**, A531 (2008).

124. R. K. Dash, J. Chmiola, G. N. Yushin, Y. Gogotsi, G. Laudisio, J. Singer, J. E. Fischer and S. Kucheyev, *Carbon*, **44**, 2489 (2006).

125. E. Hoffman, G. N. Yushin, B. M. Barsoum and G. Gogotsi, *Chem. Mater.*, **17**, 2317 (2005).

126. R. K. Dash, G. Yushin and Y. Gogotsi, *Microporous and Mesoporous Materials*, **86**, 50 (2005).

127. Z.G. Cambaz, G.N. Yushin, K.L. Vyshnyakova, L.N. Pereselentseva and Y. G. Gogotsi, *J. Am. Ceram. Soc*, **89**, 509 (2006).

128. F. Tuinstra and J. L. Koenig, *Journal of Chemical Physics*, **53**, 1126 (1970).

129. R. J. Nemanich and S. A. Solin, *Physical Review B*, **20**, 392 (1979).

130. A. C. Ferrari and J. Robertson, *Philosophical Transactions of the Royal Society a-Mathematical Physical and Engineering Sciences*, **362**, 2477 (2004).

131. S. Reich and C. Thomsen, *Philosophical Transactions of the Royal Society of London Series a-Mathematical Physical and Engineering Sciences*, **362**, 2271 (2004).

132. G. Yushin, E. Hoffman, A. Nikitin, H. Ye, M. W. Barsoum and Y. Gogotsi, *Carbon*, **44**, 2075 (2005).

133. P. L. Taberna, P. Simon and J. F. Fauvarque, *Journal of the Electrochemical Society*, **150**, A292 (2003).

134. T. E. Rufford, D. Hulicova-Jurcakova, E. Fiset, Z. H. Zhu and G. Q. Lu, *Electrochemistry Communications*, **11**, 974 (2009).

135. Z. B. Wen, Q. T. Qu, Q. Gao, X. W. Zheng, Z. H. Hu, Y. P. Wu, Y. F. Liu and X. J. Wang, *Electrochemistry Communications*, **11**, 715 (2009).